



## Inferring potential landslide damming using slope stability, geomorphic constraints and run-out analysis; case study from the NW Himalaya

Vipin Kumar<sup>1\*</sup>, Imlirenla Jamir<sup>2</sup>, Vikram Gupta<sup>3</sup>, Rajinder K. Bhasin<sup>4</sup>

<sup>1</sup>Georisks and Environment, Department of Geology, University of Liege, Liege, Belgium

<sup>2</sup>Public Works Department (PWD), Nagaland, India

<sup>3</sup>Wadia Institute of Himalayan Geology, Dehradun, India

<sup>4</sup>Norwegian Geotechnical Institute, Oslo, Norway

\*Correspondence: [v.chauhan777@gmail.com](mailto:v.chauhan777@gmail.com); B-18, B-4000, Sart-Tilman, Liege, Belgium

### 1 ABSTRACT

2 Prediction of potential landslide damming has been a difficult process owing to uncertainties  
3 related to landslide volume, resultant dam volume, entrainment, valley configuration, river  
4 discharge, material composition, friction and turbulence associated with material. In this  
5 study instability pattern of landslides, parametric uncertainty, geomorphic indices, post  
6 failure run-out predictions and spatio-temporal pattern of rainfall and earthquake is explored  
7 using Satluj valley, North-West (NW) Himalaya as a case study area to predict the potential  
8 landslide damming sites. The study area witnessed landslide damming in the past and  
9 incurred \$ ~30M loss and 350 lives in the last four decades due to such processes. Forty four  
10 active landslides in the study area that cover total  $\sim 4.81 \pm 0.05 \times 10^6 \text{ m}^2$  area and  $\sim 34.1 \pm 9.2$   
11  $\times 10^6 \text{ m}^3$  volume are evaluated in the study to identify those that may result in potential  
12 landslide damming. Out of forty four, five landslides covering the volume of  $\sim 26.3 \pm 6.7 \times$   
13  $10^6 \text{ m}^3$  are observed to form potential landslide dams. Spatio-temporal varying pattern of  
14 rainfall in recent years enhances the possibility of landslide triggering and hence potential  
15 damming. These landslides also resulted in  $24.8 \pm 2.7\text{m}$  to  $39.8 \pm 4.0\text{m}$  high material flow in  
16 run-out predictions.

17 **Key words:** Landslide damming, Slope stability; Run-out; Himalaya



## 18 1.0 INTRODUCTION

19 Landslide damming is a normal geomorphic process in narrow valleys and has been one of  
20 most disastrous natural processes (Dai et al. 2005; Gupta and Sah 2008; Delaney and Evans  
21 2015). There have been many studies that explored the damming characteristics (Li et al.  
22 1986; Costa and Schuster 1988; Takahashi and Nakawaga 1993; Ermini and Casagli 2003;  
23 Fujisawa et al. 2009; Stefanelli et al. 2016; Kumar et al. 2019a). However, studies concerning  
24 the prediction of potential landslide dams and their stability at regional scale have been  
25 relatively rare, particularly in Himalaya despite a history of landslide damming and flash  
26 floods (Gupta and Sah 2008; Ruiz-Villanueva et al. 2016; Kumar et al. 2019a). In order to  
27 identify the landslides that have potential to form dams, following factors have been main  
28 requisites; (i) pre- and post-failure behavior of landslide slopes (ii) landslide volume, stream  
29 power and morphological setting of the valley.

30 To understand the pre-failure pattern, slope stability evaluation through numerical modeling  
31 has been a common practice. The Finite Element Method (FEM) has been a most widely used  
32 numerical model for the complex slope geometry (Griffiths and Lane 1999; Jing 2003;  
33 Kanungo et al. 2013; Jamir et al. 2017; Kumar et al. 2018). However, selection of input  
34 parameters in the FEM analysis and set of assumptions (material model, failure criteria,  
35 convergence etc.) may also result into uncertainty in final output (Wong 1984; Cho 2007; Li  
36 et al. 2016; Siddique and Pradhan 2018). Input parameters based uncertainty can be resolved  
37 by performing the sensitivity/parametric analysis and utilization of most appropriate criteria  
38 can minimize the uncertainty caused by assumptions. Post-failure behavior of landslides can  
39 be understood through run-out analysis (Hungr et al. 1984; Hutter et al. 1994; Rickenmann  
40 and Scheidl 2013). These methods could be classified into empirical/statistical and dynamical  
41 categories (Rickenmann 2005). Owing to flexibility in rheology, solution approach, reference  
42 frame, and entrainment, dynamic models have been relatively more realistic for site-specific  
43 problems (Corominas and Mavrouli 2011). Though different numerical models have different  
44 advantages and limitations, Voellmy rheology (friction and turbulence) (Voellmy 1955; Salm  
45 1993) based Rapid Mass Movement Software (RAMMS) (Christen et al. 2010) model have  
46 been used widely owing to inclusion of rheological and entrainment rate flexibility.

47 Apart from pre-and post-failure pattern, landslide volume, stream power and morphological  
48 setting of the valley are crucial to infer potential landslide damming. Morphological  
49 Obstruction Index (MOI) and Hydro-morphological Dam Stability Index (HDSI) have been



50 most widely used geomorphic indices involving landslide volume, stream power and the  
51 morphological setting of valley to infer the potential of landslide dam formation and their  
52 temporal stability (Costa and Schuster 1988; Ermini and Casagli 2003; Stefanelli et al. 2016).

53 The NW Himalaya, India has been a most affected terrain by the landslides owing to active  
54 tectonics and seasonal precipitation sources i.e., Indian Summer Monsoon (ISM) and Western  
55 Disturbance (WD). The WD has been southward extension of sub-tropical westerly jet (Dimri  
56 et al. 2015). The NW Himalaya has accommodated ~51 % of all the landslides in  
57 India during yrs. 1800-2011 (Parkash 2011). The Satluj River valley, NW Himalaya is one  
58 such region that has claimed ~350 lives and loss of minimum 30 million USD due to the  
59 landslides and associated floods in the last four decades and holds a high potential for  
60 landslide damming and resultant floods (Ruiz-Villanueva et al. 2016; Kumar et al.  
61 2019a). Therefore, Satluj River valley is taken as a case study area, of which 44 landslides  
62 (20 debris slides, 13 rockfalls, and 11 rock avalanches) belonging to different litho-tectonic  
63 regimes are modeled using the FEM technique. Multiple slope sections and a range of values  
64 of different input parameters are used to perform parametric study. In order to determine the  
65 human population that may get affected by these landslides, census statistics are also used.  
66 Morphological obstruction index and Hydro-morphological dam stability index are used to  
67 determine the potential of landslide dam formation, if failure occurs, and their stability in  
68 case of formation. In view of the role of rainfall and earthquake as main landslide triggering  
69 factors, spatio-temporal regime of these two factors in the study area is also discussed. Run-  
70 out prediction of certain landslides using the RAMMS model is also performed to understand  
71 their contribution in potential landslide damming. This study provides detailed insight into  
72 regional instability pattern, associated uncertainty, and potential landslide damming sites and  
73 hence can be replicated in other hilly terrain witnessing frequent landslides and damming.

## 74 **2.0 STUDY AREA**

75 The study area is located between the Moorang ( $31^{\circ}36'1''$  N,  $78^{\circ}26'47''$  E) and Rampur town  
76 ( $31^{\circ}27'10''$  N,  $77^{\circ}38'20''$  E) of the Satluj River valley, NW Himalaya (Fig. 1). The Satluj  
77 River flows across Tethyan Sequence (TS), Higher Himalaya Crystalline (HHC), Lesser  
78 Himalaya Crystalline (LHC), and Lesser Himalaya Sequence (LHS). The TS in the study area  
79 comprises slate/phyllite and schist and has been intruded by the biotite-rich granite i.e.,  
80 Kinnaur-Kailash Granite (KKG) near the Sangla Detachment (SD) fault (Sharma 1977;  
81 Vannay et al. 2004). The SD fault separates the TS from the underlying crystalline rockmass



82 of the HHC. Migmatitic gneiss marks the upper part of the HHC whereas, base is marked by  
83 kyanite-sillimanite gneiss rockmass (Sharma 1977; Vannay et al. 2004; Kumar et al. 2019b).  
84 The Main Central Thrust (MCT) fault separates the HHC from the underlying schist/gneissic  
85 rockmass of the LHC. The LHC comprises mica schist, carbonaceous schist, quartzite, and  
86 amphibolite. A thick zone of gneiss i.e., Wangtu Gneissic Complex (WGC) is also exposed in  
87 the LHC, which comprises augen gneiss and porphyritic granitoids. The LHC is delimited at  
88 the base by the Munsiri Thrust (MT) fault that is thrust over the Lesser Himalaya  
89 Sequence (LHS) rockmass. The MT contains breccia, cataclastic, and fault gouge (Sharma  
90 1977; Vannay et al. 2004; Kumar et al. 2019b). The LHS in the study area consists of quartz-  
91 arenite (Rampur Quartzite) with bands of phyllite, meta-volcanics, and paragneiss (Sharma  
92 1977).

93 The present study covers forty-four (44) active landslides (20 debris slides, 13 rock falls, and  
94 11 rock avalanches) along the study area that have been mapped recently by Kumar et al.  
95 (2019b). The location and dimensional details of the landslides have been summarized in  
96 Table 1. Field photographs of few of these landslides are presented in Fig. 2. The TS and  
97 LHS in the study area has been subjected to tectonic tranquility with exhumation rates as low  
98 as 0.5 - 1.0 mm/yr whereas, the HHC and LHC region comprise 1.0 - 4.5 mm/yr rate of  
99 exhumation (Thiede et al. 2009; Kumar et al. 2019b). The MCT fault region and the WGC  
100 are noted to have maximum exhumation rate (i.e., ~4.5 mm/yr) that is evident from the deep  
101 gorges in these regions (Fig. 2). Further, a majority of the earthquake events in the study area  
102 in the last 7 decades have been related to the N-S oriented Kaurik - Chango Fault (KCF) that  
103 is subjected to the Karakoram Fault (KF) (Kundu et al. 2014; Hazarika et al. 2017;  
104 International Seismological Centre 2019). The climate zones in the study area also show  
105 spatial variation from humid (~800 mm/yr) in the LHS to semi-arid (~200 mm/yr) in the TS  
106 (Kumar et al. 2019b). The HHC acts as a transition zone where climate varies from semi-  
107 humid to semi-arid in SW-NE direction. This transition has been attributed to the 'orographic  
108 barrier' nature of the HHC that marks the region in its north as orographic interior and the  
109 region to its south as the orographic front (Wulf et al. 2012; Kumar et al. 2019b).

110 The landslides in the study area have been a consistent threat to the socio-economic condition  
111 of the nearby human population (Gupta and Sah 2008; Ruiz-Villanueva et al. 2016; Kumar et  
112 al. 2019a). Therefore, the human population in the vicinity of each landslide was also  
113 determined by considering villages/town in that region. It is to note that total 25,822 people  
114 reside in the 500 m radius of 44 landslide slopes and about 70 % of the this population is



115 residing in the reach of debris slide type landslides. Since the Govt. of India follows a 10 year  
116 gap in census statistics, the human population data was based on last official i.e., Census-  
117 2011. The next official census is due in 2021. It is to note that the exact population in year  
118 2020-2021 might be higher than that of census 2011 that would be reflected in census 2021.

### 119 **3.0 METHODOLOGY**

120 In order to determine the potential landslide sites along the Satluj River valley, NW  
121 Himalaya, methodology involved field data collection, satellite imagery analysis, laboratory  
122 analyses, Finite Element Method (FEM) bases slope stability evaluation, parametric analysis,  
123 application of Morphological Obstruction Index (MOI) & Hydro-morphological Dam  
124 Stability Index (HDSI) and debris run-out analysis. Details are as follows;

#### 125 *3.1 Field data, satellite imagery processing and laboratory analyses*

126 The field work involved rock/soil sample collection from each landslide location, rockmass  
127 joint mapping, and N-type Schmidt Hammer Rebound (SHR) measurement. The joints were  
128 included in the slope model for the FEM analysis. Dataset involving the joint details is  
129 uploaded to the open accessed *Mendeley Data* repository (Kumar et al. 2020). The SHR  
130 values were obtained as per International Society of Rock Mechanics (ISRM) standard  
131 (Aydin 2008).

132 The Cartosat-1satellite imagery and field assessment were used to finalize the location of  
133 slope sections (2D) of the landslides. The Cartosat-1 imagery has been used widely for  
134 landslide related studies (Martha et al. 2010). The Cartosat-1Digital Elevation Model  
135 (DEM), prepared using the Cartosat-1 stereo imagery, was used to extract the 2D slope  
136 sections of the landslides using Arc GIS-10.2 software. Details of the satellite imagery are  
137 mentioned in Table 2.

138 Rock/soil samples were analyzed in the National Geotechnical Facility (NGF) and Wadia  
139 Institute of Himalayan Geology (WIHG) laboratory, India. The rock samples were drilled and  
140 smoothed for Unconfined Compressive Strength (UCS) (IS: 9143-1979) and ultrasonic test  
141 (CATS Ultrasonic (1.95) of Geotechnical Consulting & Testing Systems. The Ultrasonic test  
142 was conducted to determine the density, elastic modulus, and Poisson's ratio of rock samples.  
143 The soil samples were tested for grain size analysis (IS: 2720-Part 4-1985), UCS test (IS:  
144 2720-Part 10-1991), and direct shear test (IS: 2720-Part 13- 1986). If the soil samples  
145 contained < 5% fines (< 75 mm), hydrometer test was not performed for the remaining fine



146 material. In the direct shear test, soil samples were sheared under constant normal stress of  
147 50, 100 and 150 kN/m<sup>2</sup>. The UCS test of soil was performed under three different rates of  
148 movements i.e., 1.25 mm/min, 1.50 mm/min and 2.5 mm/min.

### 149 3. 2 Slope stability and parametric analyses

150 The Finite Element Method (FEM) was performed along with the Shear Strength Reduction  
151 (SSR) technique to infer the critical Strength Reduction Factor (SRF), Shear Strain (SS), and  
152 Total Displacement (TD) in the 44 landslide slopes (20 debris slides, 13 rock falls, and 11  
153 rock avalanche) using the RS2 software. The SRF has been observed to be similar in nature  
154 as the Factor of Safety (FS) of the slope (Zienkiewicz et al. 1975; Griffiths and Lane 1999).  
155 To define the failure in the SSR approach, non-convergence criteria was used (Nian et al.  
156 2011). The boundary condition with the restraining movement was applied to the base and  
157 back, whereas the front face was kept free for the movement (Fig.3). In-situ field stress was  
158 adjusted in view of dominant forces i.e., extension or compression by changing the value of  
159 the coefficient of earth pressure (k). The  $k = \sigma_h/\sigma_v = 0.5$  was used in extensional regime,  
160 whereas  $k = \sigma_h/\sigma_v = 1.5$  was used in compressional regime. The spatial variability of  
161 compressional and extensional regime in this collisional orogeny region has been discussed in  
162 detail by Vannay et al. (2004).

163 The soil and rock mass were used in the FEM analysis through Mohr-Coulomb (M-C) failure  
164 criterion (Coulomb 1776; Mohr 1914) and Generalized Hoek-Brown (GHB) criterion (Hoek  
165 et al. 1995), respectively. The parallel- statistical distribution of the joints with normal-  
166 distribution joint spacing in the rock mass was applied through Barton-Bandis (B-B) slip  
167 criterion (Barton and Choubey 1977; Barton and Bandis 1990). Plane strain triangular  
168 elements having 6 nodes were used through the graded mesh in the models. Details of the  
169 criteria used in the FEM analysis are mentioned in Table 3. Dataset involving the value of  
170 input parameters used in the FEM analysis is uploaded to the open accessed *Mendeley Data*  
171 repository (Kumar et al. 2020). It is to note that the FEM analysis is performed under static  
172 load i.e., field stress and body force. The dynamic analysis is not performed, at present, in  
173 absence of any major seismic events in the region in last 4 decades (sec. 4.4) and lack of  
174 reliable dynamic load data of nearby major seismic events.

175 To understand the uncertainty caused by the selection of 2D slope section, multiple slope  
176 sections were taken, wherever possible. More than one slope sections were modeled for each  
177 debris slide, whereas for rock falls/ rock avalanche only one slope section could be chosen



178 due to the limited width of the rock falls/rock avalanche in the study area. To find out the  
179 relative influence of different input parameters on the final output, a parametric study was  
180 also performed. In the parametric study for debris slides, Akpa landslide (S.N.5 in Fig. 1),  
181 Pangi landslide (S.N.13 in Fig. 1), and Barauni Gad landslide (S.N.38 in Fig. 1) were chosen,  
182 whereas Tirung khad (S.N.2 in Fig.1) and Chagaon landslide (S.N.21 in Fig. 1) were  
183 considered to represent rock fall. Baren Dogri (S.N.7 in Fig. 1) landslide was used to  
184 represent rock avalanches. The configuration of these landslide models is presented in Fig. 3.  
185 The selection of these landslides for parametric study was based on following two factors; (1)  
186 to choose landslides from different litho-tectonic regime, (2) representation of varying stress  
187 regime i.e., extensional, compressional, and relatively stagnant. The Parametric study of the  
188 debris slide models involved following 9 parameters; field stress coefficient, stiffness ratio,  
189 cohesion and angle of friction of soil, elastic modulus and Poisson's ratio of soil, rockmass  
190 modulus, Poisson's ratio and uniaxial compressive strength of rock. For the rockfalls/rock  
191 avalanche, following 6 parameters; uniaxial compressive strength of rock, rockmass modulus  
192 of rock, Poisson's ratio of rock, 'mi' parameter, stiffness ratio, and field stress coefficient  
193 were used. The 'mi' is a Generalized Hoek-Brown (GHB) parameter that is equivalent to the  
194 angle of friction of Mohr-coulomb (M-C) criteria.

### 195 3. 3 Potential landslide dam formation & stability evaluation

196 Considering the possibility of landslide dam formation in case of slope failure, following  
197 geomorphic indices are also used;

198 (i) Morphological Obstruction Index (MOI)

$$199 \quad \text{MOI} = \log (V_1/W_v) \quad \text{Eq. 1}$$

200 (ii) Hydro-morphological Dam Stability Index (HDSI)

$$201 \quad \text{HDSI} = \log (V_d/A_b.S) \quad \text{Eq. 2}$$

202 Where,  $V_d$  (dam volume)=  $V_1$  (landslide volume),  $m^3$ ;  $A_b$  is upstream catchment area ( $km^2$ );  
203  $W_v$  is width of dammed valley (m) and  $S$  is local slope gradient of river channel (m/m).  
204 Though the resultant dam volume could be higher or lower than the landslide volume owing  
205 to slope entrainment, rockmass fragmentation, retaining of material at the slope, and washout  
206 by the river (Hung and Evans 2004; Dong et al. 2011), dam volume is assumed to be equal



207 to landslide volume for worst case. By utilizing the comprehensive dataset of ~300 landslide  
208 dams of Italy, Stefanelli et al. (2016) have classified the MOI into (i) non-formation domain:  
209 MOI <3.00 (ii) uncertain evolution domain: 3.00 <MOI >4.60 and (iii) formation domain:  
210 MOI >4.60. Similarly, utilizing the same dataset, Stefanelli et al. (2016) defined the HDSI  
211 into following categories (i) instability domain: HDSI <5.74 (ii) uncertain determination  
212 domain: 5.74<HDSI >7.44 and (iii) Stability domain: HDSI>7.44.

### 213 3. 4 Rainfall and Earthquake regime

214 Precipitation in the study area owes its existence to Indian Summer Monsoon (ISM) and  
215 Western Disturbance (WD) and varies spatially-temporally due to various localized and  
216 external factors (Gadgil et al. 2007; Hunt et al. 2018). Therefore, we have taken  
217 TRMM\_3B42 daily rainfall data of year 2000-2019 at four different locations; Moorang (in  
218 Tethyan Sequence), Kalpa (in Higher Himalaya Crystalline), Nachar (in Lesser Himalaya  
219 Crystalline) and Rampur (in Lesser Himalaya Sequence). The dataset of earthquake events  
220 (2<M<8) in and around study area during year 1940-2019 was retrieved from International  
221 Seismological Centre (ISC) catalogue (<http://www.isc.ac.uk/iscbulletin/search/catalogue/>) to  
222 determine the spatio-temporal pattern.

### 223 3. 5 Run-out analysis

224 Since the study area has witnessed many disastrous landslides, mostly rainfall triggered, and  
225 flash floods in past (Gupta and Sah 2008; Ruiz-Villanueva et al. 2016), run-out analysis was  
226 carried out to understand the post-failure scenario. Such run-out predictions will also be  
227 helpful to ascertain the possibility of damming because various studies have observed the  
228 river damming by debris flows (Li et al. 2011; Braun et al. 2018). Therefore, the landslides  
229 those have potential to form the landslide dams based on indices analysis (sec. 3.3) are  
230 evaluated for such run-out analysis.

231 In this study, Voellmy rheology (Voellmy 1955; Salm 1993) based Rapid Mass Movement  
232 Software (RAMMS) (Christen et al. 2010) model is used to understand the run-out pattern.  
233 The RAMMS for debris flow uses the Voellmy friction law and divides the frictional  
234 resistance into a dry-Coulomb type friction ( $\mu$ ) and viscous-turbulent friction ( $\xi$ ). The  
235 frictional resistance  $S$  (Pa) is thus;

$$236 \quad S = \mu N + (\rho g u^2) / \xi \quad \text{Eq. 3}$$



237 where  $N$ ;  $\rho g h \cos(\phi)$  is the normal stress on the running surface,  $\rho$ ; density,  $g$ ; gravitational  
238 acceleration,  $\phi$ ; slope angle,  $h$ ; flow height and  $u = (u_x, u_y)$ , consisting of the flow velocity in  
239 the  $x$ - and  $y$ -directions. In this study, a range of friction ( $\mu$ ) and turbulence ( $\xi$ ) values, apart  
240 from other input parameters, are used to eliminate the uncertainty in output (Table 4).  
241 Generally, the values for  $\mu$  and  $\xi$  parameters are achieved using the reconstruction of real  
242 events through simulation and subsequent comparison between dimensional characteristics of  
243 real and simulated event. However the landslides in the study area merge with the river floor  
244 and/or are in close proximity and there is no failed material left from previous events to  
245 reconstruct. Therefore,  $\mu$  and  $\xi$  values were taken in a range in view of topography of  
246 landslide slope and run-out path, landslide material, similar landslide events/material and  
247 based on previous studies/models (Hurlimann et al. 2008; Rickenmann and Scheidl 2013;  
248 RAMMS v.1.7.0). Since these landslides are relatively deep in nature and we are of  
249 understanding that during slope failure, irrespective of type of trigger, entire loose material  
250 might not slide down, the depth of landslide is taken as only  $\frac{1}{4}$  (thickness) in the run-out  
251 calculation.

## 252 4.0 RESULTS

### 253 4.1 Slope instability regime and parametric output

254 Results indicated that out of 44 landslides (20 debris slides, 13 rockfalls, and 11 rock  
255 avalanches), 31 are in meta-stable state ( $1 \leq FS \leq 2$ ) and 13 in unstable state ( $FS < 1$ ) (Fig. 4).  
256 Most of the unstable landslides are debris slides, whereas the majority of the meta-stable  
257 landslides ( $1 \leq FS \leq 2$ ) are rock fall/rock avalanche. Debris slides constitute  $\sim 90\%$  and  $\sim 99\%$   
258 of the total area and volume, respectively of the unstable landslides. It is to note that about  
259  $\sim 70\%$  of the total human population along the study area resides in the vicinity ( $\sim 500$  m) of  
260 these unstable debris slides (Fig. 4). Rock falls/Rock avalanches constitute  $\sim 84\%$  and  $\sim 78\%$   
261 of the area and volume, respectively of the meta-stable landslides. Out of total twenty debris  
262 slides, twelve debris slides are found to be in unstable ( $FS < 1$ ) stage whereas, eight in meta-  
263 stable condition ( $1 < FS < 2$ ) (Fig. 4). These twenty debris slides occupy  $\sim 1.9 \pm 0.02 \times 10^6$  m<sup>2</sup>  
264 area and  $\sim 26 \pm 6 \times 10^6$  m<sup>3</sup> volume. While comparing the factor of safety with the Total  
265 Displacement (TD) and Shear Strain (SS), nonlinear poor correlation is achieved (Fig. 5).  
266 Since, the TD and SS present a relatively good correlation (Fig. 5), only the TD is used  
267 further alongwith the FS. The TD ranges from  $7.4 \pm 8.9$  cm to  $95.5 \pm 10$  cm for unstable debris  
268 slides and  $\sim 18.8$  cm for meta-stable landslides (Fig. 4).



269 Out of thirteen (13) rockfalls, one (1) belongs to the unstable state ( $FS < 1$ ) and twelve (12) to  
270 the meta-stable state ( $1 < FS < 2$ ) (Fig. 4). The TD varies from 0.4 to 8.0 cm with the  
271 maximum for Bara Kamba rockfall (S.N. 31 in Fig. 1) in the Lesser Himalaya Crystalline.  
272 Out of eleven (11) rock avalanches, one (1) belongs to the unstable state ( $FS < 1$ ) and ten (10)  
273 to the meta-stable state ( $1 < FS < 2$ ) (Fig. 4). The TD varies from 6.0 to 132.0 cm with the  
274 maximum for the Kandar rock avalanche (S.N. 25 in Fig. 1) of the Lesser Himalaya  
275 Crystalline. It is noteworthy that relatively higher TD is obtained by the rock fall and rock  
276 avalanche of the Lesser Himalaya Crystalline region (Fig. 4). The landslides of the Higher  
277 Himalaya Crystalline (HHC), Kinnaur Kailash Granite (KKG) and Tethyan Sequence (TS),  
278 despite being only 17 out of the total 44 landslides, constituted  $\sim 67\%$  and  $\sim 82\%$  of the total  
279 area and total volume of the landslides.

280 The Factor of Safety (FS) of debris slides is found to be relatively less sensitive to the change  
281 in the value of input parameters than the Total Displacement (TD) (Fig. 6). In case of Akpa  
282 ('a' in Fig. 6) and Pangi landslide ('b' in Fig. 6), soil friction and field stress have more  
283 influence on the FS. However, for the TD, field stress, elastic modulus and Poisson's ratio of  
284 soil are relatively more controlling parameters. The FS and TD of the Barauni Gad landslide  
285 ('c' in Fig. 6) are relatively more sensitive to soil cohesion and 'mi' parameter. Therefore, it  
286 can be inferred that the FS of debris slides is more sensitive to soil friction and field stress,  
287 whereas TD is mostly controlled by field stress and deformation parameters i.e, elastic  
288 modulus and Poisson's ratio. Similar to the debris slides, the FS of rock falls and rock  
289 avalanche are found to be relatively less sensitive than TD to the change in the value of input  
290 parameters (Fig. 7). In case of Chagaon rock fall ('c' in Fig. 7), poission ratio and UCS have  
291 relatively more influence on FS and TD. Tirung Khad rock fall ('a' in Fig. 7) and Baren  
292 Dogri rock avalanche ('b' in Fig. 7) show dominance of 'mi' parameter and field stress in the  
293 FS as well as in TD. Thus, it can be inferred that the rock fall/rock avalanche are more  
294 sensitive to 'mi' parameter and field stress.

#### 295 *4.2 Potential landslide damming*

296 Based on the MOI, out of total 44 landslides, 5 (S.N. 5, 7, 14, 15, 19) are observed to be in  
297 formation domain, 15 in uncertain domain and 24 in non-formation domain, at present (Fig.  
298 8a). These five landslides that have potential to dam the river in case of slope failure  
299 accommodate  $\sim 26.3 \pm 6.7 \times 10^6 \text{ m}^3$  volume (Fig. 8). The five landslides are also presented  
300 separately in Fig. 9 (a-e).



301 In terms of temporal stability (or durability), out of five landslides that have potential to block  
302 the river, only one landslide (S.N. 5) is noted to attain the uncertain domain, whereas  
303 remaining four show instability (Fig. 8b,d). The lacustrine deposit in the upstream of Akpa  
304 landslide (S.N. 5) in Fig. 9a implies the signs of landslide damming in the past too (Fig. 10).  
305 The uncertain temporal stability indicates that the landslide dam may be stable or unstable  
306 depending upon the stream power and landslide volume, which in turn are dynamic factors  
307 and may change owing to changing climate and/or tectonic event. The landslides that have  
308 been observed to form the landslide dam but are noted to be in temporally unstable category  
309 (S.N. 7, 14, 15, 19) are still considerable owing to associated risks of lake-impoundment and  
310 generation of secondary landslides. Urni landslide (S.N. 19) (Fig. 9e) that damaged the part  
311 of National Highway road (NH)-05 has already partially dammed the river since year 2016  
312 and holds potential for further damming (Kumar et al. 2019a). Apart from S.N. 5 and S.N. 19  
313 landslides, remaining landslides (S.N. 7, 14, 15 in Fig. 1) belong to Higher Himalaya  
314 Crystalline (HHC) region that has been observed to accommodate many landslide damming  
315 and subsequent flash floods events in the past (Sharma et al. 2017).

#### 316 *4.3 Rainfall and Earthquake regime*

317 In order to explain the spatio-temporal variation in rainfall, topographic profile of the study  
318 area is plotted along with the rainfall variation (Fig. 11a). The temporal distribution of  
319 rainfall is presented at annual, monsoonal (SW Indian Monsoon: June-September) and non-  
320 monsoonal (Western Disturbance: Oct-May) level (Fig. 11b-d). Rainfall data of year 2000-  
321 2019 revealed a relative increase in annual rainfall since year 2010 (Fig. 11b). The Kalpa  
322 region (situated in orographic barrier setting) received relatively more annual rainfall than the  
323 Rampur, Nachar and Moorang region throughout the time period, except year 2017. The  
324 rainfall dominance at Kalpa is more visible in non-monsoonal season (Fig. 11d). It may be  
325 due to its orographic influence on the saturated winds of western disturbance. Further, the  
326 rainfall during the monsoon season that was dominant at the Rampur region till year 2012  
327 gained dominance at Kalpa region since year 2013 (Fig. 11c).

328 Extreme rainfall events of June 2013 that resulted in widespread slope failure in the NW  
329 Himalaya also caused landslide damming at places (NDMA 2013; Kumar et al. 2019a).  
330 Similar to the year 2013 rainfall event, the year 2007, 2010 and 2019 also witnessed  
331 enhanced annual rainfall and associated flash floods and/or landslides in the region  
332 (hpenvis.nic.in, retrieved on March 1, 2020; sandrp.in, retrieved on March 1, 2020).



333 However, the contribution of ISM season rainfall and WD associated rainfall has been  
334 variable in these years (Fig. 11). Such frequent but inconsistent rainfall events that possess  
335 varied (temporally) dominance of ISM and WD are observed to owe their occurrence to  
336 following local and regional factors; El-Nino Southern Oscillation (ENSO), Equatorial Indian  
337 Ocean Circulation (EIOC) and planetary warming (Gadgil et al. 2007; Hunt et al. 2018).  
338 Orographic setting is noted to act as principle local factor as evident from relatively more  
339 rainfall (total precipitation= $1748\pm 594$  mm/yr.) at Kalpa region (orographic barrier) in the  
340 non-monsoon and monsoon season from the year 2010 onwards (Fig. 11). Prediction of  
341 potential landslide damming sites in the region revealed that four (S.N. 7, 14, 15, 19) out of  
342 five landslides that can form the dam belong to this orographic barrier. Therefore, in view of  
343 the prevailing rainfall trend since the year 2010, regional factors, discussed above, and  
344 orographic setting, precipitation triggered slope failure events cannot be denied in the future.  
345 Such slope failure events, if occurred, at the predicted landslide damming sites may certainly  
346 dam the river.

347 The seismic pattern revealed that the region has been hit by 1662 events with epicenters  
348 located in and around the study area (Fig. 12a). However,  $\sim 99.5\%$  of these earthquake events  
349 had a magnitude of less than 6.0 and only 8 events are recorded in the range of 6.0 to 6.8  $M_s$ ,  
350 (International Seismological Centre 2019). Out of these 8 events, only one event i.e., 6.8  $M_s$ ,  
351 (19<sup>th</sup> Jan. 1975) has been noted to induce widespread slope failures in the study area (Khattri  
352 et al. 1978). The majority of the earthquake events in the study area has occurred in the  
353 vicinity of the N-S oriented trans-tensional Kaurik - Chango Fault (KCF) that accommodated  
354 the epicenter of 19<sup>th</sup> Jan. 1975 earthquake (Hazarika et al. 2017; International Seismological  
355 Centre 2019). It is to note that about 95% of total 1662 events had their focal depth within 40  
356 km (Fig. 12b). Such a relatively low magnitude - shallow seismicity in the region has been  
357 related to the Main Himalayan Thrust (MHT) decollement as a response to relatively low  
358 convergence ( $\sim 14\pm 2$  mm/yr) of India and Eurasia plates in this region (Bilham 2019) (Fig.  
359 12c). Further, the arc (Himalaya)-perpendicular Delhi-Haridwar ridge that is underthrusting  
360 Eurasian plate in this region has been observed to be responsible for the spatially varied *low*  
361 seismicity in the region (Hazarika et al. 2017). Thus, though the study area has been  
362 subjected to low magnitude-shallow seismicity, chances of earthquake-triggered landslides  
363 have been relatively low in comparison to rainfall-triggered landslides and associated  
364 landslide damming. For this reason and lack of reliable dynamic load of major earthquake



365 event, we have performed the *static* modeling in the present study. However, we intend to  
366 perform the *dynamic* modeling in near future if reliable dynamic load data will be available.

#### 367 4.4 Run-out analysis

368 All five landslides (S.N. 5, 7, 14, 15, 19 in Fig. 8, 9) that are observed to form potential  
369 landslide dam in the event of slope failure were also considered for the run-out analysis.  
370 Results are as follows;

##### 371 4.4.1 Akpa landslide (S.N. 5)

372 Though it is difficult to ascertain that how much part of the debris flow might contribute in  
373 the river blockage, it will certainly block the river in view of ~38 m high debris material with  
374 ~50 m wide run-out across the channel in this narrow part of river valley (Fig. 9a) even at  
375 maximum value of coefficient of friction (i.e.,  $\mu = 0.3$ ) (Fig. 13a). It is to note that not only  
376 the run-out extent but flow height also decreases on increasing friction value (Fig. 13a.1-  
377 13.a.3). The maximum friction can take into account the possible resistance by vegetation on  
378 slope and bed-load on river channel. However, apart from the frictional characteristics of run-  
379 out path, saturation of debris flow also controls its dimension and hence consequences like  
380 potential damming. To account the saturation of debris flow, different values of turbulence  
381 coefficient ( $\xi$ ) were used (Table 4). The resultant flow height (representing 9 sets of debris  
382 flow obtained using  $\mu = 0.05, 0.1$  and  $0.3$  and  $\xi = 100, 200$  and  $300 \text{ m/s}^2$ ) attains its peak value  
383 i.e.,  $39.8 \pm 4.0 \text{ m}$  at the base of central part of landslide (Fig. 14a).

##### 384 4.4.2 Baren dogri landslide (S.N. 7)

385 At the maximum friction value ( $\mu = 0.4$ ), Baren dogri landslide is noted to attain peak value of  
386 flow height i.e., ~30 m at the base of central part of landslide (Fig. 13b). Similar to the valley  
387 configuration around the Akpa landslide (sec 4.4.1), river valley attains narrow/deep gorge  
388 setting here also (Fig. 9b). The maximum value of debris flow height obtained using different  
389  $\mu$  and  $\xi$  values is  $25.6 \pm 2.1 \text{ m}$  (Fig. 14b). Flow material is also noted to attain more run-out in  
390 upstream direction of river (~1100 m) than in the downstream direction (~800 m). This  
391 spatial variability in run-out length might exist due to river channel configuration as river  
392 channel in upstream direction is relatively narrower than the downstream direction.

##### 393 4.4.3 Pawari landslide (S.N. 14)



394 Pawari landslide attains maximum flow height of  $\sim 20$  m at the maximum friction of run-out  
395 path ( $\mu=0.4$ ) (Fig. 13c). The resultant debris flow that is achieved using different values of  $\mu$   
396 and  $\xi$  parameters attains a peak value of  $24.8 \pm 2.7$  m and decreases gradually with a run-out  
397 of  $\sim 1500$  m in upstream and downstream direction (Fig. 14c). This landslide resulted in the  
398 relatively long run-out of  $\sim 1500$  m in upstream and downstream direction. Apart from the  
399 landslide volume that affects the run-out extent, valley morphology also controls it as evident  
400 from previous landslides. The river channel in upstream and downstream direction from the  
401 landslide location is observed to be narrow (Fig. 9c).

#### 402 *4.4.4 Telangi landslide (S.N. 15)*

403 Telangi landslide is noted to result in peak debris flow height of  $\sim 24$  m at the maximum  
404 friction ( $\mu=0.4$ ) (Fig. 13d). It is to note that on increasing the friction of run-out path, flow  
405 run-out decreased along the river channel but increased across the river channel resulting into  
406 possible damming. The debris flow after taking into account different values of  $\mu$  and  $\xi$   
407 parameters attains a peak value of  $25.0 \pm 4.0$  m (Fig. 14d). Similar to Baren dogri landslide  
408 (S.N. 7), material attained more run-out in upstream direction of river ( $\sim 1800$  m) than in  
409 downstream direction ( $\sim 600$  m) that attributes to narrower river channel in upstream than the  
410 downstream direction. The downstream side attains wider river channel due to the traversing  
411 of Main Central Thrust (MCT) fault in the proximity (Fig. 1). Since Pawari and Telangi  
412 landslide (S.N 14 & 15) are situated  $\sim 500$  m from each other, their respective flow run-outs  
413 might mix in the river channel resulting into disastrous cumulative effect.

#### 414 *4.4.5 Urni landslide (S.N. 19)*

415 Urni landslide attained a peak value of  $\sim 44$  m of debris flow height at the maximum friction  
416 value ( $\mu=0.4$ ) (Fig. 13e). After taking into account different values of  $\mu$  and  $\xi$  parameters, the  
417 debris flow attained a height of  $26.3 \pm 1.8$  m (Fig. 14e). Relatively wider river channel in  
418 downstream direction (Fig. 9e) is considered to result in long run-out in downstream  
419 direction than in the upstream.

## 420 **5.0 DISCUSSION**

421 Present study aimed to determine the potential landslide damming sites in the Satluj River  
422 valley, NW Himalaya. In order to achieve this objective, 44 landslides along the Satluj River  
423 valley were considered. At first, slope stability evaluation of all slopes was performed  
424 alongwith parametric evaluation. Then geomorphic indices i.e., Morphological Obstruction



425 Index (MOI) and Hydro-morphological Dam Stability Index (HDSI) were used to predict the  
426 formation of potential landslide dam and their subsequent stability. Rainfall and earthquake  
427 regime were also explored in the study area. Finally, run-out analysis was performed of those  
428 landslides that have been observed to form potential landslide dam.

429 The MOI revealed that out of forty-four landslides, five (S.N. 5, 7, 14, 15, 19) have potential  
430 to form the landslide dam (Fig. 8, 9). On evaluating the stability of such potential dam sites  
431 using the HDSI, the landslide (S.N. 5) is noted to attain uncertain domain ( $5.74 < \text{HDSI} < 7.44$ )  
432 in terms of dam stability. The uncertain term implies that the resultant dam may be stable or  
433 unstable depending upon the landslide/dam volume, upstream catchment area (or water  
434 discharge) and slope gradient (sec 3.3). Since this landslide presents clear signs of having  
435 already formed a dam in the past, as indicated by the alternating fine-coarse layered sediment  
436 deposit (or lake deposit) in the upstream region (Fig. 9a, 10), recurrence can't be denied.  
437 Further, run-out analysis of landslide has predicted  $39.8 \pm 4.0\text{m}$  high debris flow in the event  
438 of failure that will block the river completely (Fig. 13a, 14a). However, the durability of the  
439 blocking can't be ascertained as it subjected to the volume of landslide that will be retained at  
440 the channel and river discharge.

441 Remaining four landslides (S.N. 7, 14, 15, 19), though showed instability i.e.,  $\text{HDSI} < 5.74$  at  
442 present, may form the dam in near future as the region accommodating these landslides has  
443 been affected by such damming and subsequent flash floods in the past (Sharma et al. 2017).  
444 The last one of these i.e., S.N. 19 (Urni landslide) has already dammed the river partially and  
445 holds potential to completely block the river in near future (Kumar et al. 2019a). Run-out  
446 analysis of these landslides (S.N. 7, 14, 15, 19) has predicted  $25.6 \pm 2.1\text{m}$ ,  $24.8 \pm 2.7\text{m}$ ,  $25.0 \pm$   
447  $4.0\text{m}$  and  $26.3 \pm 1.8\text{m}$  flow height, respectively that will result in temporary blocking of the  
448 river (Fig. 13,14). These findings of run-out indicate towards the blocking of river in the  
449 event of slope failure, irrespective of durability, despite the conservative depth as input  
450 because only  $\frac{1}{4}$  of landslide thickness is used in the run-out analysis (sec. 3.5).

451 Stability evaluation of these five landslide slopes (S.N. 5, 7, 14, 15, 19) that have potential to  
452 form landslide dam revealed that except one landslide (S.N.7) that is meta-stable ( $1 \leq \text{FS} \leq 2$ ),  
453 at present, remaining four belong to unstable category ( $\text{FS} < 1$ ) (Fig. 4). Further, except this  
454 landslide that is meta-stable (S.N. 7), remaining four unstable landslide slopes is debris slide  
455 in nature. It is noteworthy to discuss the implications of  $\text{FS} < 1$ . The Factor of safety (FS) in  
456 the Shear Strength Reduction (SSR) approach is a factor by which the existing shear strength



457 of material is divided to determine the critical shear strength at which failure occurs  
458 (Zienkiewicz et al. 1975; Duncan 1996). Since the landslide represents a failed slope i.e.,  
459 critical shear strength > existing shear strength,  $FS < 1$  is justifiable. Further, the failure state  
460 of a slope in the FEM can be defined by different criteria; the FS of same slope may vary a  
461 little depending upon the usage of failure criteria and convergence threshold (Abramson et al.  
462 1996; Griffiths and Lane 1999).

463 In general, the possible causes of instability ( $FS < 1$ ) may be steep slope gradient, weak  
464 lithology, and jointed rock mass. Three (S.N. 7, 14, 15) out of these five landslides that have  
465 potential to form the dam belong to the tectonically active Higher Himalaya Crystalline  
466 (HHC) and the notion of steep slope gradient cannot be generalized because the HHC  
467 accommodates most voluminous ( $\sim 10^5$ - $10^7$  m<sup>3</sup>) landslides (Fig. 4). These deep seated  
468 landslides must require smooth slope gradient to accommodate the voluminous overburden.  
469 The HHC comprises strong lithology i.e., gneiss therefore, therefore the notion of weak  
470 lithology also may not be appropriate. However, the jointed rock mass that owes its origin to  
471 numerous small scale folds, shearing and faults associated with the active orogeny process  
472 (sec.2.0) can be considered as the main factor for relatively more instability of debris slide  
473 type landslides. Since, the study area is subjected to the varied stress regime caused by the  
474 tectonic structures (Vannay et al. 2004) thermal variations (Singh et al. 2015), and  
475 anthropogenic cause (Lata et al. 2015), joints may continue to develop and destabilize the  
476 slopes. Apart from this inherent factor like joints, external factors like rainfall and  
477 exhumation rate may also contribute to instability of these landslides. This region receives  
478 relatively more annual rainfall owing to orographic barrier setting (Fig. 11) and is subjected  
479 to relatively high exhumation rate of 2.0-4.5 mm/yr (Thiede et al. 2009).

480 Two landslides (S.N. 5, 19) that are also capable to form potential landslide dam (Fig. 8, 9a;  
481 e) and are also unstable ( $FS < 1$ ) in nature (Fig. 4) do not belong to the HHC. The first  
482 landslide (S.N. 5) exists at the lithological contact of schist and Kinnaur Kailash Granite  
483 (KKG) rockmass and regional normal fault i.e., Sangla Detachment (ST) or South Tibetan  
484 Detachment (STD) passes through this contact. Few studies suggest that the SD normal fault  
485 is an outcome of reactivation of former thrust fault (Vannay et al. 2004) that has resulted in  
486 intense rockmass shearing (Kumar et al. 2019b). Owing to its location in orographic interior  
487 region, hillslopes receives very low annual rainfall (Fig. 11) and thus comprises least  
488 vegetation on hillslope. The lack of vegetation on hillslopes has been observed to result in



489 low shear strength of material and hence in instability (Kokutse et al. 2016). Thus,  
490 lithological contrast, rockmass shearing and lack of vegetation are the main reasons of  
491 instability of S.N. 5 landslide. The second landslide (S.N. 19) belongs to inter-layered  
492 schist/gneiss rockmass of the Lesser Himalaya Crystalline (LHC) and is situated at  
493 orographic front where rainfall increases suddenly (Fig. 11). Further, this region is also  
494 subjected to high exhumation rate of 2.0-4.5 mm/yr (Thiede et al. 2009). Therefore,  
495 lithological contrast, high rainfall and high exhumation rate are considered as the main  
496 reasons of instability of this landslide slope.

497 The landslides that could not result into river damming on the basis of volume and valley  
498 characteristics are mostly in the LHC and Lesser Himalaya Sequence (LHS) region. These  
499 regions consist of a majority of rock fall and rock avalanche type landslides that are generally  
500 of meta-stable ( $1 \leq FS \leq 2$ ) category (Fig. 4). Despite the deep/narrow valley setting, landslides  
501 in these regions may not form the potential landslide dam, at present, owing to relatively less  
502 landslide volume. The possible causes of meta-stability ( $1 \leq FS \leq 2$ ) of rock fall and rock  
503 avalanche may be strong lithology (gneissic), dense vegetation on the hillslopes (Chawla et  
504 al. 2012), relatively less sheared rock mass in comparison to the HHC region, and relatively  
505 less decrease in land use/landcover (Lata et al. 2015). Maximum Total Displacement (TD) is  
506 also associated with the rock fall and rock avalanche of this region (Fig. 4).

507 In the parametric study, soil friction and in-situ stress are noted to affect the FS most in case  
508 of debris slide, whereas the FS of rock fall and rock avalanche are mainly controlled by 'mi'  
509 i.e., (a Generalized Hoek-Brown criteria parameter) and the in-situ stress. For the TD of the  
510 debris slides, field stress, elastic modulus and Poisson's ratio, whereas for rock falls and rock  
511 avalanches, 'mi' parameter and in-situ stress play the dominant role (Fig. 6,7). Soil friction  
512 ( $\phi$ ) has been a controlling factor for the shear strength and its decrease has been observed to  
513 result in the shear failure of slope material (Matsui and San 1992). The 'm<sub>i</sub>' (a GHB  
514 parameter), an equivalent of the angle of friction of the M-C envelope is observed to  
515 dominate the FS and TD of the rock fall. Since the rainfall constitutes an important role in  
516 decreasing the friction of slope material through percolation and change the pore water  
517 pressure regime (Rahardjo et al. 2005), a relatively high frequency of extreme rainfall events  
518 in the Satluj River valley since the year 2013 (Kumar et al. 2019a) amplifies the risk of  
519 hillslope instability. Furthermore, the in-situ field stress that has been compressional and/or  
520 extensional owing to orogenic setting in the region may also enhance hillslope instability



521 (Eberhardt et al. 2004; Vannay et al. 2004). Deformation parameters e.g. elastic modulus and  
522 Poisson's ratio are also observed to affect the displacement in slope models of the debris  
523 slides. Similar studies in other regions have also noted the sensitivity of the elastic modulus  
524 and Poisson's ratio on the slope stability (Zhang and Chen 2006).

525 The study area has been subjected to frequent excessive rainfalls since the year 2010 and  
526 received widespread slope failures and flash-floods (Fig. 11b). Three (S.N. 7,14,15 in Fig. 9)  
527 out of five potential landslide dams that are predicted belong to the Higher Himalaya  
528 Crystalline (HHC) that receives relatively more rainfall (Fig. 11). Previous studies have also  
529 noted that the most of the landslide dams in the river valley had originated in the HHC region  
530 and climatic factors, particularly rainfall, was the most probable reason for the slope failures  
531 (Sharma et al. 2017). The earthquake, however, has been second to rainfall as the triggering  
532 factor for slope failures in the study area. Contrary to the along 'Himalayan' arc distribution  
533 of earthquakes, the study area has received most of the earthquakes around the Kaurik-  
534 Chango Fault only (Fig. 12a). However, the only major earthquake event has been M 6.8  
535 earthquake on 19<sup>th</sup> Jan. 1975 that resulted in widespread landslides (Khattari et al. 1978).  
536 About ~99.5 % of the earthquake events that occurred during the years 1940-2019 in and  
537 around study area had their magnitude less than 6.0 and about ~95 % of all events originated  
538 within 40 km. Such low magnitude seismicity has been attributed to the northward extension  
539 of the Delhi-Haridwar ridge (Hazarika et al. 2019) whereas, shallow seismicity is subjected to  
540 the MHT ramp structure in the region that allows strain accumulation at shallow depth  
541 (Bilham 2019). Thus, earthquake has not been a major landslide triggering process in the  
542 region.

543 In view of the possible uncertainties in the predictive nature of study, following assumptions  
544 and then resolutions were made;

- 545 • To account the effect the spatial variability in slope geometry in the FEM analysis, 3D  
546 models have been in use for the last decade (Griffiths and Marquez 2007). However,  
547 the pre-requisite for the 3D FEM involves the detailed understanding of slope  
548 geometry and material variability in the subsurface that was not possible in the study  
549 area considering steep and inaccessible slopes. Therefore, multiple 2D sections were  
550 chosen, wherever possible. To account the effect of sampling bias and material  
551 variability, a range of values of input parameters was used (sec. 3.4).



- 552 • Determination of the debris thickness has been a major problem in landslide volume  
553 measurement particularly in steep, narrow river valleys of the NW Himalaya where  
554 landslide scarps are not accessible. Therefore, the thickness was approximated by  
555 considering the relative altitude of the ground on either side of the deposit, as also  
556 performed by Innes (1983). It was assumed that the ground beneath the deposit is  
557 regular.
- 558 • The resultant dam volume could also be different from the landslide volume due to  
559 entrainment of slope material during movement, rockmass fragmentation, pore water  
560 pressure, size of debris particles, and washout of landslide material by the river  
561 (Hung and Evans 2004; Dong et al. 2011; Yu et al. 2014). Therefore, dam volume is  
562 presumed to be equal to landslide volume for the worst case scenario and least  
563 associated uncertainty (sec. 3.5).
- 564 • Stream power that is manifested by upstream catchment area and local slope gradient  
565 may also vary at temporal scale owing to temporally varying water influx from  
566 glaciers and precipitation systems i.e., Indian Summer Monsoon and Western  
567 Disturbance (Gadgil et al. 2007; Hunt et al. 2018). Though our study is confined to  
568 spatial scale at present, the findings remain subjected to the change at temporal scale.
- 569 • The Voellmy rheology based RAMMS model (Voellmy 1955; Salm 1993; Christen et  
570 al. 2010) requires calibrated friction ( $\mu$ ) and turbulence ( $\xi$ ) values for the run-out  
571 analysis. Though the previous run-out events don't have trace in the study area owing  
572 to convergence of landslide toe with the river channel, a range of  $\mu$  and  $\xi$  values were  
573 used in the study in view of material type and run-out path.

574 Despite these uncertainties, such studies are required to minimize the risk and avert the  
575 possible disasters in terrains where human population is bound to live in the proximity of  
576 unstable landslides.

## 577 CONCLUSIONS

578 Out of forty four landslides that are studied, five landslides are observed to form potential  
579 landslide dam, if failure occurs. Though the blocking duration is difficult to predict, upstream  
580 and downstream consequences of these damming events can't be overlooked as the region  
581 has witnessed many damming and flash floods in the past that resulted in widespread loss of  
582 lives and economy.



583 These five landslides comprise a total landslide volume of  $26.3 \pm 6.7 \text{ M m}^3$ . The slopes of  
584 four landslides (debris slides) out of these five are unstable i.e., Factor of safety  $< 1$  whereas,  
585 remaining one (rock avalanche) is meta-stable i.e.,  $1 \leq \text{FS} \leq 2$ . Field observations and previous  
586 studies have noted the damming events by these landslides (or the region consisting these  
587 landslides) in the past too. Since the area is witnessing enhanced rainfall and flash floods  
588 since year 2010, findings of the run-out analysis that involve  $24.8 \pm 2.7\text{m}$  to  $39.8 \pm 4.0\text{m}$  high  
589 material flow from these landslides become more crucial.

590 In order to evaluate the sensitivity of factor of safety and total displacement in slope stability  
591 analysis, parametric study was performed. The angle of internal friction of soil or ' $m_i$ ' (a  
592 parameter of the Generalized Hoek Brown criteria that is equivalent to the angle of internal  
593 friction) of rockmass and *in-situ* field stress are noted to be the most controlling parameters  
594 for the stability of slopes.

#### 595 **Conflict of Interest**

596 The authors declare that they have no conflict of interest.

#### 597 **Dataset Availability**

598 The dataset (Joints and value of input parameters used in the FEM analysis) is deposited in  
599 approved open access repository (*Mendeley data*) as Kumar et al. (2020).

#### 600 **Author contribution**

601 VK collected the field data. VK and IJ performed the laboratory analysis. All authors  
602 contributed to the dataset compilation, numerical modeling (Slope stability and Run-out) and  
603 geomorphic interpretations. All authors contributed to the writing of final draft.

#### 604 **ACKNOWLEDGEMENT**

605 The authors are thankful to the Director, Wadia Institute of Himalayan Geology (WIHG) for  
606 all the necessary support. VK and IJ acknowledge constructive discussion on the regional  
607 scale study with Prof. H.B. Havenith, Prof. D.V. Griffiths, and Prof. D.P. Kanungo. VG and  
608 RKB acknowledge the financial help through project MOES/Indo-Nor/PS-2/2015. Authors  
609 are thankful to the RAMMS developer for the license.

#### 610 **REFERENCES**



- 611 Abramson, L. W., Lee, T. S., Sharma, S. 1996. "Slope stability and stabilization methods".  
612 New York. Wiley.
- 613 Aydin, A. 2008. "ISRM suggested method for determination of the Schmidt hammer rebound  
614 hardness: revised version". In: R. Ulusay (ed) *The ISRM Suggested Methods for Rock  
615 Characterization, Testing and Monitoring: 2007–2014*. Springer, Cham, pp. 25-33.
- 616 Barton, N. and Bandis, S. 1982. "Effects of block size on the shear behavior of jointed rock".  
617 In: *Proc. 23rd US symposium on rock mechanics*. American Rock Mechanics  
618 Association, 739-760.
- 619 Barton, N. and Choubey, V. 1977. "The shear strength of rock joints in theory and practice".  
620 *Rock mechanics* 10(1-2):1-54.
- 621 Barton, N. R. 1972. "A model study of rock-joint deformation. International journal of rock  
622 mechanics and mining sciences". *Geomech. Abstr.* 9 (5): 579-602.
- 623 Barton, N. R. and Bandis, S. C. 1990. "Review of predictive capabilities of JRC-JCS model in  
624 engineering practice". In: *Barton N and Stephansson O (ed) Rock Joints*, Rotterdam,  
625 pp. 603-610.
- 626 Bhasin, R. and Kaynia, A. M. 2004. "Static and dynamic simulation of a 700-m high rock  
627 slope in western Norway". *Engineering Geology* 71(3-4): 213-226.
- 628 Bilham, R. 2019. "Himalayan earthquakes: a review of historical seismicity and early 21st  
629 century slip potential". *Geological Society, London, Special Publications*. 483(1):423-  
630 82.
- 631 Bowles, J. E. 1996. *Foundation Analysis and Design, 5<sup>th</sup> ed.*, McGraw-Hill, New York, pp.  
632 750.
- 633 Braun, A., Cuomo, S., Petrosino, S., Wang, X. and Zhang, L., 2018. "Numerical SPH  
634 analysis of debris flow run-out and related river damming scenarios for a local case  
635 study in SW China". *Landslides* 15 (3), 535-550.
- 636 Cai, M., Kaiser, P. K., Tasaka, Y. and Minami, M. 2007. "Determination of residual strength  
637 parameters of jointed rock masses using the GSI system". *International Journal of Rock  
638 Mechanics and Mining Sciences* 44(2): 247-265.
- 639 Chawla, A., Kumar, A., Lal, B., Singh, R.D. and Thukral, A.K. 2012. "Ecological  
640 Characterization of High Altitude Himalayan Landscapes in the Upper Satluj River  
641 Watershed, Kinnaur, Himachal Pradesh, India". *Journal of the Indian Society of Remote  
642 Sensing* 40(3): 519-539.
- 643 Cho, S. E. 2007. "Effects of spatial variability of soil properties on slope stability".  
644 *Engineering Geology* 92(3-4): 97-109.
- 645 Christen, M., Kowalski, J., Bartelt, P. 2010. "RAMMS: Numerical simulation of dense snow  
646 avalanches in three-dimensional terrain". *Cold Regions Science and Technology*. 63: 1-  
647 14.
- 648 Corominas, J. and Mavrouli, J., 2011. "Living with landslide risk in Europe: Assessment,  
649 effects of global change, and risk management strategies". *Documento tecnico,  
650 safeland. 7<sup>th</sup> Framework Programme Cooperation Theme*, 6.
- 651 Costa, J. E. and Schuster, R. L. 1988. "The formation and failure of natural dams". *Geological  
652 society of America bulletin* 100(7): 1054-1068.



- 653 Coulomb, C. A. 1776. "An attempt to apply the rules of maxima and minima to several  
654 problems of stability related to architecture". *Mémoires de l'Académie Royale des*  
655 *Sciences* 7: 343-382.
- 656 Dai, F.C., Lee, C.F., Deng, J.H. and Tham, L.G. 2005. "The 1786 earthquake-triggered  
657 landslide dam and subsequent dam-break flood on the Dadu River, southwestern  
658 China". *Geomorphology* 65(3): 205-221.
- 659 Deere, D. U. and Miller, R. P. 1966. "Engineering classification and index properties for  
660 intact rock". Illinois University at Urbana, USA.
- 661 Delaney, K. B. and Evans, S. G. 2015. "The 2000 Yigong landslide (Tibetan Plateau),  
662 rockslide-dammed lake and outburst flood: review, remote sensing analysis, and  
663 process modelling". *Geomorphology* 246, 377-393.
- 664 Dimri, A.P., Niyogi, D., Barros, A.P., Ridley, J., Mohanty, U.C., Yasunari, T. and Sikka,  
665 D.R. 2015. "Western disturbances: A review". *Reviews of Geophysics* 53(2): 225-246
- 666 Dong, J.J., Tung, Y.H., Chen, C.C., Liao, J.J. and Pan, Y.W. 2011. "Logistic regression model  
667 for predicting the failure probability of a landslide dam". *Engineering Geology* 117(1):  
668 52-61.
- 669 Duncan, J. M. 1996. "State of art: limit equilibrium and finite element analysis of slopes".  
670 *Journal of Geotechnical Engineering Division, ASCE* 122 (7): 577-596.
- 671 Eberhardt, E., Stead, D. and Coggan, J. S. 2004. "Numerical analysis of initiation and  
672 progressive failure in natural rock slopes—the 1991 Randa rockslide". *International*  
673 *Journal of Rock Mechanics and Mining Sciences* 41(1): 69-87.
- 674 Ermini, L. and Casagli, N. 2003. "Prediction of the behaviour of landslide dams using a  
675 geomorphological dimensionless index". *Earth Surface Processes and Landforms*  
676 28(1): 31-47.
- 677 Fujisawa, K., Kobayashi, A. and Aoyama, S. 2009. "Theoretical description of embankment  
678 erosion owing to overflow". *Geotechnique* 59(8): 661-671.
- 679 Gadgil, S., Rajeevan, M. and Francis, P.A. 2007. "Monsoon variability: Links to major  
680 oscillations over the equatorial Pacific and Indian oceans". *Current Science*. 93(2):182-  
681 94.
- 682 Griffiths, D. V. and Lane, P. A. 1999. "Slope stability analysis by finite elements".  
683 *Geotechnique* 49(3): 387-403.
- 684 Griffiths, D. V. and Marquez, R. M. 2007. "Three-dimensional slope stability analysis by  
685 elasto-plastic finite elements". *Geotechnique* 57(6): 537-546.
- 686 Gupta, V. and Sah, M. P. 2008. "Impact of the trans-Himalayan landslide lake outburst flood  
687 (LLOF) in the Satluj catchment, Himachal Pradesh, India". *Natural Hazards* 45(3):  
688 379-390.
- 689 Gupta, V., Nautiyal, H., Kumar, V., Jamir, I., and Tandon, R. S. 2016. "Landslides hazards  
690 around Uttarkashi Township, Garhwal Himalaya, after the tragic flash flood in June  
691 2013". *Natural Hazards* 80: 1689-1707
- 692 Hürlimann, M., Rickenmann, D., Medina, V. and Bateman, A. 2008. "Evaluation of  
693 approaches to calculate debris-flow parameters for hazard assessment". *Eng Geol*  
694 102:152-163



- 695 Havenith, H.B., Torgoev, I. and Ischuk, A. 2018. “Integrated Geophysical-Geological 3D  
696 Model of the Right-Bank Slope Downstream from the Rogun Dam Construction Site,  
697 Tajikistan”. *International Journal of Geophysics* 1-17.
- 698 Hazarika, D., Wadhawan, M., Paul, A., Kumar, N. and Borah, K. 2017. “Geometry of the  
699 Main Himalayan Thrust and Moho beneath Satluj valley, northwest Himalaya:  
700 Constraints from receiver function analysis”. *Journal of Geophysical Research: Solid  
701 Earth*. 122(4):2929-45.
- 702 Hoek, E. and Brown, E.T. 1997. “Practical estimates of rock mass strength”. *International  
703 Journal of Rock Mechanics and Mining Science* 34(8):1165-1186
- 704 Hoek, E. and Diederichs, M.S. 2006. “Empirical estimation of rock mass modulus”.  
705 *International Journal of Rock Mechanics and Mining Sciences* 43 (2): 203-15.
- 706 Hoek, E., Kaiser, P.K. and Bawden, W.F. 1995. *Support of Underground Excavations in Hard  
707 Rock*. Rotterdam: A. A. Balkema.
- 708 Hungr, O. and Evans, S.G. 2004. “Entrainment of debris in rock avalanches: an analysis of a  
709 long run-out mechanism”. *Geological Society of America Bulletin* 116(9-10): 1240-  
710 1252.
- 711 Hungr, O., Morgan, G.C. and Kellerhals, R. 1984. “Quantitative analysis of debris torrent  
712 hazards for design of remedial measures”. *Can Geotech J* 21:663–677
- 713 Hunt, K.M., Turner, A.G. and Shaffrey, L.C. 2018. “The evolution, seasonality and impacts of  
714 western disturbances”. *Quarterly Journal of the Royal Meteorological Society*.  
715 144(710):278-90.
- 716 Hutter, K., Svendsen, B. and Rickenmann, D. 1994. “Debris flow modelling: a review”.  
717 *Continuum mechanics and thermodynamics* 8: 1-35.
- 718 Innes, J. L. 1983. “Debris flows”. *Progress in Physical Geography* 7(4): 469–501.
- 719 IS: 2720 (Part 10)–1991. “Method of test for soils: Determination of unconfined compressive  
720 strength”. In: *Bureau of Indian Standards, Delhi, India*.
- 721 IS: 2720 (Part 13)–1986. “Method of test for soils: Direct shear test”. In: *Bureau of Indian  
722 Standards, New Delhi, India*.
- 723 IS: 2720 (Part 4)–1985. “Methods of test for soils: Grain size analysis”. In: *Bureau of Indian  
724 Standards, New Delhi, India*.
- 725 IS: 9143-1979. “Method for the determination of unconfined compressive strength of rock  
726 materials”. In: *Bureau of Indian Standards, New Delhi, India*.
- 727 Jamir, I., Gupta, V., Kumar, V. and Thong, G.T. 2017. “Evaluation of potential surface  
728 instability using finite element method in Kharsali Village, Yamuna Valley, Northwest  
729 Himalaya”. *Journal of Mountain Science* 14(8): 1666-1676.
- 730 Jamir, I., Gupta, V., Thong, G.T. and Kumar, V. 2019. “Litho-tectonic and precipitation  
731 implications on landslides, Yamuna valley, NW Himalaya”. *Physical Geography* 41(4)  
732 365-388.
- 733 Jang, H.S., Kang, S.S. and Jang, B.A. 2014. “Determination of joint roughness coefficients  
734 using roughness parameters”. *Rock mechanics and rock engineering* 47(6): 2061-73.
- 735 Jing, L. 2003. “A review of techniques, advance and outstanding issues in numerical  
736 modelling for rock mechanics and rock engineering”. *International Journal of Rock  
737 Mechanics and Mineral Science* 40:283-353.



- 738 Kanungo, D.P., Pain, A. and Sharma, S. 2013. "Finite element modeling approach to assess  
739 the stability of debris and rock slopes: a case study from the Indian Himalayas". *Natural*  
740 *hazards* 69(1): 1-24.
- 741 Khattri, K., Rai, K., Jain, A.K., Sinval, H., Gaur, V.K. and Mithal, R.S. 1978. "The Kinnaur  
742 earthquake, Himachal Pradesh, India, of 19 January, 1975". *Tectonophysics*. 49(1-2):1-  
743 21.
- 744 Kokutse, N.K., Temgoua, A.G.T. and Kavazović, Z. 2016. "Slope stability and vegetation:  
745 Conceptual and numerical investigation of mechanical effects". *Ecological Engineering*  
746 86: 146–153.
- 747 Kumar, V., Gupta, V. and Jamir, I. 2018. "Hazard Evaluation of Progressive Pawari Landslide  
748 Zone, Kinnaur, Satluj Valley, Higher Himalaya, India". *Natural Hazards* 93: 1029-  
749 1047.
- 750 Kumar, V., Gupta, V., Jamir, I. and Chatteraj, S.L. 2019a. "Evaluation of potential landslide  
751 damming: Case study of Urni landslide, Kinnaur, Satluj valley, India". *Geosci. Front.*  
752 10(2): 753-767.
- 753 Kumar, V., Gupta, V. and Sundriyal, Y.P. 2019b. "Spatial interrelationship of landslides,  
754 litho-tectonics, and climate regime, Satluj valley, Northwest Himalaya". *Geol. J.* 54:  
755 537–551.
- 756 Kumar, V., Jamir, I., Gupta, V. and Bhasin, R.K. 2020. "Dataset used to infer regional slope  
757 stability, NW Himalaya". *Mendeley Data*. DOI: 10.17632/jh8b2rh8nz.1
- 758 Kundu, B., Yadav, R.K., Bali, B.S., Chowdhury, S. and Gahalaut, V.K. 2014. "Oblique  
759 convergence and slip partitioning in the NW Himalaya: Implications from GPS  
760 measurements." *Tectonics* 33: 2013-2024.
- 761 Lata, R., Rishi, S., Talwar, D. and Dolma, K. 2015. "Comparative Study of Landuse Pattern in  
762 the Hilly Area of Kinnaur District, Himachal Pradesh, India". *International Journal of*  
763 *Innovative Science, Engineering & Technology* 2(4): 559-565.
- 764 Li, D.Q., Qi, X.H., Cao, Z.J., Tang, X.S., Phoon, K.K. and Zhou, C.B. 2016. "Evaluating  
765 slope stability uncertainty using coupled Markov chain". *Computers and*  
766 *Geotechnics* 73:72-82.
- 767 Li, T., Schuster, R.L. and Wu, J. 1986. "Landslide dams in south-central China". In: *Proc.*  
768 *Landslide dams: processes, risk, and mitigation*, ASCE Convention, Washington, 146-  
769 162.
- 770 Li, M.H., Sung, R.T., Dong, J.J., Lee, C.T., and Chen, C.C. 2011. "The formation and  
771 breaching of a short-lived landslide dam at Hsiaolin village, Taiwan-Part II: Simulation  
772 of debris flow with landslide dam breach". *Engineering Geology* 123: 60-71.
- 773 Martha, T.R., Kerle, N., Jetten, V., van Westen, C.J. and Kumar, K.V. 2010. "Landslide  
774 volumetric analysis using Cartosat-1-derived DEMs". *IEEE Geoscience and remote*  
775 *sensing letters* 7(3): 582-586.
- 776 Matsui, T. and San, K.C. 1992. "Finite element slope stability analysis by shear strength  
777 reduction technique". *Soils and foundations* 32(1): 59-70.
- 778 Mohr, O. 1914. "Abhandlungen aus dem Gebiete der Technischen Mechanik" (2nd ed). Ernst,  
779 Berlin.
- 780 NDMA: National Disaster Management Authority. 2013. Annual report, Government of  
781 India, Delhi.



- 782 Nian, T.K., Chen, G.Q., Wan, S.S. and Luan, M.T. 2011. "Non-convergence Criterion on  
783 Slope Stability FE Analysis by Strength Reduction Method". *Journal of Convergence*  
784 *Information Technology* 6:78-88.
- 785 O'Brien, J.S., Julien, P.Y. and Fullerton, W.T. 1993. "Two-dimensional water flood and mud  
786 flood simulation". *J Hydraul Eng* 119:244–260.
- 787 Parkash, S. 2011. "Historical records of socio-economically significant landslides in India". *J*  
788 *South Asia Disaster Studies* 4(2): 177-204.
- 789 Rahardjo, H., Lee, T.T., Leong, E.C. and Rezaur, R.B. 2005. "Response of a residual soil  
790 slope to rainfall". *Canadian Geotechnical Journal* 42(2): 340-351.
- 791 Rickenmann, D. 2005. "Runout prediction methods". In: *Jakob M, Hungr O (eds) Debris-flow*  
792 *hazards and related phenomena*. Praxis/Springer, Berlin/Heidelberg, pp. 305–324.
- 793 Rickenmann, D., and Scheidl, C. 2013. "Debris-Flow Runout and Deposition on the Fan". *M.*  
794 *Schneuwly-Bollschweiler et al. (eds.), Dating Torrential Processes on Fans and Cones,*  
795 *Advances in Global Change Research* 47, DOI 10.1007/978-94-007-4336-6 5
- 796 Ruiz-Villanueva, V., Allen, S., Arora, M., Goel, N. K. and Stoffel, M. 2016. "Recent  
797 catastrophic landslide lake outburst floods in the Himalayan mountain range". *Progress*  
798 *in Physical Geography* 41 (1): 3-28.
- 799 Salm, B., 1993. "Flow, flow transition and runout distances of flowing avalanches". *Ann.*  
800 *Glaciol.* 18: 221–226.
- 801 Sharma, S., Shukla, A.D., Bartarya, S.K., Marh, B.S. and Juyal, N. 2017. "The Holocene  
802 floods and their affinity to climatic variability in the western Himalaya, India".  
803 *Geomorphology* 290: 317–334.
- 804 Sharma, K. K. 1977. "A contribution to the geology of Satluj Valley, Kinnaur, Himachal  
805 Pradesh, India". *Collques Internationaux du CNRS* 268: 369-378.
- 806 Siddque, T. and Pradhan, S. P. 2018. "Stability and sensitivity analysis of Himalayan road cut  
807 debris slopes: an investigation along NH-58, India". *Natural Hazards* 93(2): 577-600.
- 808 Singh, D., Gupta, R.D. and Jain, S.K. 2015. "Statistical analysis of long term spatial and  
809 temporal trends of temperature parameters over Sutlej river basin, India". *J. Earth Syst.*  
810 *Sci.* 124 (1): 17-35.
- 811 Stefanelli, C.T., Segoni, S., Casagli, N. and Catani, F. 2016. "Geomorphic indexing of  
812 landslide dams evolution". *Engineering Geology* 208: 1-10.
- 813 Takahashi, T. And Nakagawa, H. 1993. "Flood and debris flow hydrograph due to collapse of  
814 a natural dam by overtopping". In: *Proc. Hydraulic Engineering, Japan*, 37: 699-704.
- 815 Thiede, R.C., Ehlers, T.A., Bookhagen, B. and Strecker, M.R. 2009. "Erosional variability  
816 along the northwest Himalaya". *Journal of Geophysical Research: Earth Surface* 114  
817 F101015.
- 818 Vannay, J.C., Grasemann, B., Rahn, M., Frank, W., Carter, A., Baudraz, V. and Cosca, M.  
819 2004. "Miocene to Holocene exhumation of metamorphic crustal wedges in the NW  
820 Himalaya: Evidence for tectonic extrusion coupled to fluvial erosion". *Tectonics* 23  
821 TC1014.
- 822 Voellmy, A. 1955. "On the destructive force of avalanches", *Translation No. 2. Avalanche*  
823 *Study Center, United States Department of Agriculture, USA.*
- 824 Wong, F.S. 1984. "Uncertainties in FE modeling of slope stability". *Computers & structures*  
825 19(5-6): 777-791.



- 826 Wulf, H., Bookhagen, B. and Scherler, D. 2012. "Climatic and geologic controls on  
827 suspended sediment flux in the Sutlej River Valley, western Himalaya". *Hydrology and*  
828 *Earth System Sciences* 16(7): 2193-2217.
- 829 Yu, G., Zhang, M., Chen, H., 2014. "The dynamic process and sensitivity analysis for debris  
830 flow". In: *Sassa, K., Canuti, P., Yin, Y. (Eds.), Landslide Science for a Safer*  
831 *Geoenvironment*. Springer.
- 832 Zhang, P. W. and Chen, Z. Y. 2006. "Influences of soil elastic modulus and Poisson's ratio on  
833 slope stability". *YantuLixue (Rock and Soil Mechanics)* 27(2): 299-303.
- 834 Zienkiewicz, O. C., Humpheson, C. and Lewis, R. W. 1975. "Associated and non-associated  
835 viscoplasticity and plasticity in soil mechanics". *Geotechnique* 25(4): 671-689.

### 836 LIST OF FIGURES AND TABLES

837 **Fig. 1** Geological setting. TS, HHC, LHC and LHS are Tethyan Sequence, Higher Himalaya  
838 Crystalline, Lesser Himalaya Crystalline and Lesser Himalaya Sequence, respectively.  
839 WGC: Wangtu Gneissic Complex. Geological setting is based on Sharma (1977);  
840 Vannay et al., (2001); Kumar et al., (2019b). The red dashed circle in the inset  
841 represents the region within 100 km radius from the Satluj River (marked as blue line)  
842 that was used to determine the earthquake distribution in the area. KCF in inset refers to  
843 Kaurik-Chango Fault. The numbers 1-44 refer to serial number of landslides.

844 **Fig. 2** Field photographs of some of the landslides (a) Khokpa landslide (S.N.1); (b)  
845 Akpa\_III landslide (S.N. 5); (c) Rarang landslide (S.N. 6); (d) Pawari landslide (S.N.14);  
846 (e) Urni landslide (S.N.19); (f) Barauni Gad\_I\_S landslide(S.N. 38). Black circle in the  
847 pictures that encircles the vehicle is intended to represent the relative scale.

848 **Fig. 3** The FEM configuration of some of the slope models. S.N. refers to serial no. of  
849 landslides in Table 1. The joint distribution model in all the slopes was parallel statistical  
850 with normal distribution of joint spacing.

851 **Fig. 4** The FEM analysis of all forty-four landslides. Grey bar in the background highlights  
852 the Higher Himalaya Crystalline (HHC) region that comprises relatively more unstable  
853 landslides, relatively more landslide volume and human population. Source of human  
854 population: Census 2011 (Govt. of India, New Delhi). TS, KKG, HHC, LHC and LHS  
855 are Tethyan Sequence, Kinnaur Kailash Granite, Higher Himalaya Crystalline, Lesser  
856 Himalaya Crystalline and Lesser Himalaya Sequence, respectively



857 **Fig. 5** Relationship of Factor of Safety (FS), Total Displacement (TD) and Shear Strain (SS).  
858 DS, RF, and RA refer to Debris slide, rock fall and rock avalanche, respectively.

859 **Fig. 6** Parametric analysis of debris slides. (a) Akpa\_III (S.N. 5): (b) Pangi\_III (S.N. 13): (c)  
860 Barauni Gad\_I\_S(S.N. 38). S. N. refers to serial no. of landslides in Table 1.

861 **Fig. 7** Parametric analysis of rockfall/rock avalanche. (a) Tirung khad (S.N. 2): (b) Baren  
862 Dogri (S.No. 7): (c) Chagaon\_II (S.N. 21).

863 **Fig. 8** Landslide damming indices (a) Morphological Obstruction Index (MOI); (b) Hydro-  
864 morphological dam stability index (HDSI); (c) Landslides vs. MOI; (d) Landslides vs.  
865 HDSI.

866 **Fig. 9** Potential landslide damming locations. (a) Akpa\_III landslide; (b) Baren dogri  
867 landslide; (c) Pawari landslide; (d) Telangi landslide; (e) Urni landslide. S. N. refers to  
868 serial no. of landslides in Table 1.

869 **Fig. 10** Field signatures of the landslide damming near Akpa\_III landslide. (a) Upstream view  
870 of Akpa landslide with lacustrine deposit at the left bank; (b) enlarged view of lacustrine  
871 deposit with arrow indicating lacustrine sequence; (c) alternating fine-coarse sediments.  
872 F and Crefer to fine (covered by yellow dashed lines) and coarse (covered by green  
873 dashed lines) sediments, respectively.

874 **Fig. 11** Rainfall distribution. (a) Topographic profile; (b) annual rainfall; (c) monsoonal  
875 (June-Sep.) rainfall; (d) non-monsoonal (Oct.-May) rainfall. Green bars represent years  
876 of relatively more rainfall resulting into flash floods, landslides and socio-economic loss  
877 in the region. (i):hpennis.nic.in, retrieved on March 1, 2020; Department of Revenue,  
878 Govt. of H.P. (ii): hpennis.nic.in, retrieved on March 1, 2020.(iii): Kumar et al.,  
879 2019a;ndma.gov.in, retrieved on march 1, 2020 (iv):sandrp.in, retrieved on march 1,  
880 2020.The numbers 1-44 refer to serial number of landslides.

881 **Fig. 12** Earthquake distribution. (a) Spatial variation of earthquakes. The transparent circle  
882 represents the region within 100 km radius from the Satluj River (blue line). The black  
883 dashed line represents the seismic dominance around Kaurik-Chango fault;(b)  
884 earthquake magnitude vs. focal depth. The red dashed region highlights the  
885 concentration of earthquakes within 40 km depth. ISC: International Seismological



886 Centre; (c) Cross section view (Based on Hazarika et al. 2017; Bilham, 2019). Red  
887 dashed circle represents the zone of strain accumulation caused by the Indian and  
888 Eurasian plate collision. SD, MCT, MT, MBT and HFT are Sangla Detachment, Main  
889 Central Thrust, Munsiri Thrust, Main Boundary Thrust and Himalayan Frontal Thrust,  
890 respectively.

891 **Fig. 13** Results of run-out analysis.  $\mu$  refers to coefficient of friction. S. N. refers to serial no.  
892 of landslides in Table 1

893 **Fig. 14** Results of run-out analysis at different values of  $\mu$  and  $\xi$ .  $\mu$  and  $\xi$  refer to coefficient  
894 of friction and turbulence, respectively.

895 **Table 1** Details of landslides used in the study.

896 **Table 2** Details of satellite imagery.

897 **Table 3** Criteria used in the Finite Element Method (FEM) analysis.

898 **Table 4** Details of input parameters used in run-out analysis.



S.N.	Landslide location	Latitude/ Longitude	Type	Area <sup>1</sup> , m <sup>2</sup>	Volume <sup>2</sup> , m <sup>3</sup>	Human population <sup>3</sup>	Litho- tectonic division
1	Khokpa	31°35'18.9"N 78°26'28.6"E	Debris slide	21897± 241	43794± 18361	373	Tethyan Sequence (TS)
2	Tirung Khad	31°34'50.4"N 78°26'20.5"E	Rockfall	28537± 314	14269± 9055	0	
3	Akpa_I	31°34'57.1"N 78°24'30.6"E	Rock avalanche	963051± 10594	1926102± 807515	0	TS-KKG
4	Akpa_II	31°35'2.2"N 78°23'25.4"E	Rock avalanche	95902± 1055	143853± 40734	470	Kinnaur Kailash Granite (KKG)
5	Akpa_III	31°34'54.5"N 78°23'2.4"E	Debris slide	379570± 4175	7591400± 3182681	1617	
6	Rarang	31°35'58.7"N 78°20'39.1"E	Rockfall	4586± 50	4586± 1923	848	Higher Himalaya Crystalline (HHC)
7	Baren Dogri	31°36'23.6"N 78°20'23.1"E	Rock avalanche	483721± 5321	2418605±421561	142	
8	Thopan Dogri	31°36'12.3"N 78°19'50.4"E	Rockfall	55296± 608	165888± 46974	103	
9	Kashang Khad_I	31°36'5.0"N 78°18'44.4"E	Debris slide	113054± 1244	169581± 48019	103	
10	Kashang Khad_II	31°35'58.3"N 78°18'34.0"E	Rockfall	27171± 299	40757± 11541	103	
11	Pangi_I	31°35'36.4"N 78°17'36.4"E	Debris slide	30112± 331	45168± 12790	1389	
12	Pangi_II	31°35'38.9"N 78°17'12.2"E	Debris slide	59436± 654	118872± 49837	1389	
13	Pangi_III	31°34'38.9"N 78°16'55.6"E	Debris slide	75396± 829	188490± 32854	7	
14	Pawari	31°33'49.8"N 78°16'28.6"E	Debris slide	320564± 3526	1602820± 279370	4427	
15	Telang	31°33'7.0"N 78°16'37.2"E	Debris slide	543343± 5977	13583575± 2367608	6817	
16	Shongthong	31°31'13.0"N 78°16'17.0"E	Debris slide	5727± 63	11454± 2464	388	
17	Karchham	31°30'12.4"N 78°11'30.8"E	Rock avalanche	28046± 309	56092± 23516	0	Lesser Himalaya Crystalline (LHC)
18	Choling	31°31'17.0"N 78° 8'4.9"E	Debris slide	20977± 231	20977± 8795	0	
19	Urni	31°31'8.0"N 78° 7'42.2"E	Debris slide	112097± 1233	1120970± 469965	500	
20	Chagaon_I	31°30'55.9"N 78° 6'52.0"E	Rockfall	3220± 35	3220± 1350	0	
21	Chagaon_II	31°30'57.9"N 78° 6'47.7"E	Rockfall	11652± 128	11652± 4885	0	



22	Chagaon_III	31°31'3.0"N 78° 6'21.4"E	Debris slide	42141± 464	168564± 70670	1085	
23	Wangtu_U/s	31°32'4.8"N 78° 3'5.0"E	Rock avalanche	211599± 2328	317399± 89876	17	
24	Wangtu D/s_1	31°33'27.7"N 77°59'43.7"E	Debris slide	4655± 51	9310± 3903	71	
25	Kandar	31°33'43.7"N 77°59'54.9"E	Rock avalanche	151128± 1662	302256± 126720	186	
26	Wangtu D/s_2	31°33'38.9"N 77°59'29.9"E	Debris slide	8004± 88	16008± 6711	71	
27	Agade	31°33'52.3"N 77°58'3.5"E	Debris slide	9767± 107	14651± 4149	356	
28	Punaspa	31°33'37.6"N 77°57'31.5"E	Debris slide	3211± 35	3211± 1346	343	
29	Sungra	31°33'58.8"N 77°56'49.6"E	Debris slide	5560± 61	11120± 4662	2669	
30	Chota Kamba	31°33'39.2"N 77°54'39.0"E	Rock avalanche	197290± 2170	591870± 167597	401	
31	Bara Kamba	31°34'10.4"N 77°52'56.7"E	Rockfall	36347± 400	18174± 7619	564	
32	Karape	31°33'44.9"N 77°53'13.9"E	Debris slide	50979± 561	50979± 21373	1118	
33	Pashpa	31°34'40.2"N 77°50'53.0"E	Rockfall	16079± 171	8040± 3371	29	
34	Khani Dhar_I	31°33'43.4"N 77°48'52.5"E	Rock avalanche	218688± 2406	874752± 366738	0	
35	Khani Dhar_II	31°33'26.3"N 77°48'35.8"E	Rock avalanche	146994± 1617	734970± 248125	0	
36	Khani Dhar_III	31°33'20.1"N 77°48'27.8"E	Rock avalanche	20902± 230	62706± 17756	0	
37	Jeori	31°31'58.8"N 77°46'18.2"E	Rock avalanche	93705± 1031	93705± 39286	0	
38	Barauni Gad_I_S	31°28'56.6"N 77°41'40.4"E	Debris slide	63241± 696	758892± 111620	236	LHC-LHS
39	Barauni Gad_I_Q	31°29'00.0"N 77°41'38.0"E	Debris slide	59273± 652	711276± 104616	0	
40	Barauni Gad_II	31°28'43.9"N 77°41'24.6"E	Rockfall	6977± 77	3489± 1463	0	
41	Barauni Gad_III	31°29'5.6"N 77°41'23.7"E	Rockfall	33115± 364	33115± 13883	0	
42	D/s Barauni Gad_I	31°28'24.9"N 77°41'8.4"E	Rockfall	19101± 210	19101± 8008	0	
43	D/s Barauni Gad_II	31°28'25.5"N 77°40'56.7"E	Rockfall	21236± 234	21236± 8903	0	
44	D/s Barauni Gad_III	31°28'7.4"N 77°40'42.4"E	Rockfall	15632± 172	15632± 6554	0	Lesser Himalaya Sequence (LHS)



<sup>1</sup>Error ( $\pm$ ) caused by GE measurement (1.06 %).

<sup>2</sup>Error ( $\pm$ ) is an outcome of multiplication of area  $\pm$  error and thickness  $\pm$  error. Thickness error (Std. dev.) corresponds to averaging of field based approximated thickness.

<sup>3</sup>The human population is based on census 2011, Govt. of India. The villages/town in the radius of 500 m from the landslide are considered to count the human population.

**Table 1** Details of landslides used in the study.



Satellite data		Source	Date of data	Spatial resolution
CARTOSAT-1 stereo imagery	524/253	National Remote Sensing Center (NRSC), Hyderabad, India	5 <sup>th</sup> Dec. 2010	~2.5 m
	525/253		16 <sup>th</sup> Dec. 2010	~2.5 m
	526/252		18 <sup>th</sup> Oct. 2011	~2.5 m
	526/253		18 <sup>th</sup> Oct. 2011	~2.5 m
	527/252		24 <sup>th</sup> Nov. 2010	~2.5 m
	527/253		27 <sup>th</sup> Dec. 2010	~2.5 m
	528/252		26 <sup>th</sup> Nov. 2011	~2.5 m

**Table 2** Details of satellite imagery.



**Table 3** Criteria used in the Finite Element Method (FEM) analysis.

	Material Criteria	Parameters	Source
Rockmass	<p><b>Generalized Hoek &amp; Brown (GHB) Criteria</b>                      (Hoek et al. 1995)</p> $\sigma_1 = \sigma_3 + \sigma_{ci} [m_b (\sigma_3 / \sigma_{ci}) + s]^a$ <p>Here, <math>\sigma_1</math> and <math>\sigma_3</math> are major and minor effective principal stresses at failure; <math>\sigma_{ci}</math>, compressive strength of intact rock; <math>m_b</math>, a reduced value of the material constant (<math>m_i</math>) and is given by;</p> $m_b = m_i e^{(GSI-100)/(28-14D)}$ <p>s and a; constants for the rock mass given by the following relationships;</p> $s = e^{(GSI-100)/(9-3D)}$ $a = \frac{1}{2} + \frac{1}{6} \left[ e^{-\frac{GSI}{15}} - e^{-\frac{20}{3}} \right]$ <p>Here, D; a factor which depends upon the degree of disturbance to which the rock mass has been subjected by blast damage and stress relaxation. GSI (Geological Strength Index); a rockmass characterization parameter.</p>	Unit Weight, $\gamma$ (MN/m <sup>3</sup> )	Laboratory analysis (UCS) (IS: 9143-1979)
		Uniaxial Compressive Strength, $\sigma_{ci}$ (MPa)	
		Rockmass modulus (MPa)	Laboratory analysis (Ultrasonic velocity test); Hoek and Diederichs (2006).
		Poisson's Ratio	
		Geological Strength Index	Field observation and based on recent amendments (Cai et al. 2007 and reference therein)
		Material Constant ( $m_i$ )	Standard values (Hoek and Brown 1997)
		$m_b$	GSI was field dependent, $m_i$ as per (Hoek and Brown 1997) and D is used between 0-1 in view of rockmass exposure and blasting.
		s	
		a	
		D	
Joint	<p><b>Barton-Bandis Criteria</b>                      (Barton and Choubey 1977; Barton and Bandis 1990)</p> $\tau = \sigma_n \tan [\phi_r + JRC \log_{10} (JCS / \sigma_n)]$ <p>Here, <math>\tau</math> is joint shear strength; <math>\sigma_n</math>, normal stress across joint; <math>\phi_r</math>, reduced friction angle; JRC, joint roughness coefficient; JCS, joint compressive strength.</p> <p>JRC is based on the chart of Barton and Choubey (1977); Jang et al. (2014). JCS was determined using following equation;</p> $\log_{10}(JCS) = 0.00088 (R_L)(\gamma) + 1.01$ <p>Here, <math>R_L</math> is Schimdt Hammer Rebound value and <math>\gamma</math> is unit weight of rock.</p> <p>The JRC and JCS were used as <math>JRC_n</math> and <math>JCS_n</math> following the scale corrections observed by Barton and</p>	Normal Stiffness, $k_n$ (MPa/m)	$E_i$ is lab dependent. $L$ and GSI were field dependent. D is used between 0-1 in view of rockmass exposure and blasting.
		Shear Stiffness, $k_s$ (MPa/m)	It is assumed as $k_n/10$ . However, effect of denominator is also obtained through parametric study.
		Reduced friction angle, $\phi_r$	Standard values (Barton and Choubey 1977).
		Joint roughness coefficient, JRC	Field based data from profilometer and standard values from Barton and Choubey (1977); Jang et al. (2014).



	<p>Choubey (1977) and reference therein and proposed by Barton and Bandis (1982).</p> $JRC_n = [JRC(L/L_o)^{-0.02(JRC)}]$ $JCS_n = [JCS(L/L_o)^{-0.03(JRC)}]$ <p>Here, <math>L</math> and <math>L_o</math> are mean joint spacing in field and, respectively. <math>L_o</math> has been suggested to be 10 cm.</p> <p style="text-align: center;"><b>Joint stiffness criteria</b> (Barton 1972)</p> $k_n = (E_i * E_m) / L * (E_i - E_m)$ <p>Here, <math>k_n</math>; Normal stiffness, <math>E_i</math>; Intact rock modulus, <math>E_m</math>; Rockmass modulus <math>L</math>; Mean joint spacing.</p> $E_m = (E_i) * [0.02 + \{1 - D/2\} / \{1 + e^{(60 + 15 * D - GSI)/11}\}]$ <p>Here, <math>E_m</math> is based on Hoek and Diederichs (2006) and reference therein</p>	Joint compressive strength, JCS (MPa)	Empirical equation of Deere and Miller (1966) relating Schmidt Hammer Rebound (SHR) values, $\sigma_{ci}$ and unit weight of rock. SHR was field dependent.
		Scale corrected, $JRC_n$	Empirical equation of Barton and Bandis (1982).
		Scale corrected, $JCS_n$ (MPa)	
	Soil	<p style="text-align: center;"><b>Mohr-Coulomb Criteria</b> (Coulomb 1776; Mohr 1914)</p> $\tau = C + \sigma \tan \phi$ <p>Here, <math>\tau</math>; Shear stress at failure, <math>C</math>; Cohesion, <math>\sigma_n</math>; normal strength, <math>\phi</math>; angle of friction.</p>	Unit Weight ( $MN/m^3$ )
		Young's Modulus, $E_i$ (MPa)	Laboratory analysis (UCS); IS: 2720-Part 10-1991.
		Poisson's Ratio	Standard values from Bowles (1996)
		Cohesion, $C$ (MPa)	Laboratory analysis (Direct shear)
		Friction angle, $\phi$	(IS: 2720-Part 13- 1986)



Landslide	Material type	Material depth <sup>1</sup> , m	Friction coefficient <sup>2</sup>	Turbulence coefficient <sup>3</sup> , m/sec <sup>2</sup>
Akpa (S.N. 5)	Gravelly sand	5	$\mu = 0.05, 0.1, 0.3$	$\xi = 100, 200, 300$
Baren Dogri (S.N. 7)	Gravelly sand	1.25	$\mu = 0.05, 0.1, 0.4$	$\xi = 100, 200, 300$
Pawari (S.N. 14)	Gravelly sand	1.25	$\mu = 0.05, 0.1, 0.4$	$\xi = 100, 200, 300$
Telangi (S.N. 15)	Gravelly sand	6.25	$\mu = 0.05, 0.1, 0.4$	$\xi = 100, 200, 300$
Urni (S.N. 19)	Gravelly sand	2.5	$\mu = 0.06, 0.1, 0.4$	$\xi = 100, 200, 300$

<sup>1</sup> Considering that fact that during slope failure, irrespective of type of trigger, entire loose material might not slide down, the depth is taken as only  $\frac{1}{4}$  (thickness) in the calculation. <sup>2</sup> Since the angle of run-out track (slope and river channel) varied a little beyond the suggested range  $2.8^\circ - 21.8^\circ$  or  $\mu = 0.05 - 0.4$  (Hung et al., 1984; RAMMS v.1.7.0), we kept out input in this suggested range wherever possible to avoid simulation uncertainty. <sup>3</sup> This range is used in view of the type of loose material i.e., granular in this study (RAMMS v.1.7.0).

**Table 4** Details of input parameters for run-out analysis. S.N. refers to serial number of landslides in Fig. 1.

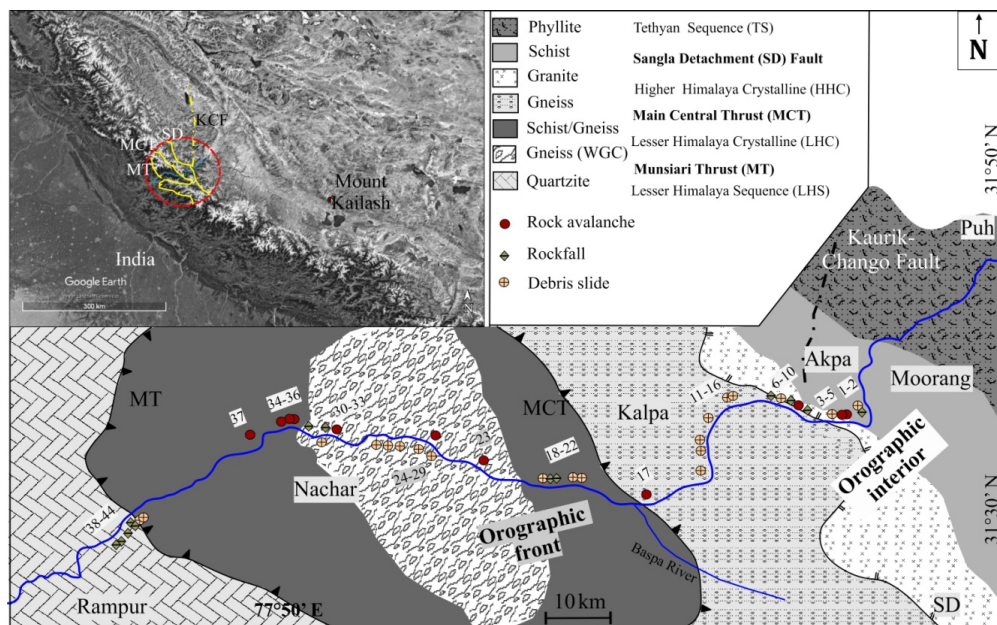


**Fig. 1** Geological setting. TS, HHC, LHC and LHS are Tethyan Sequence, Higher Himalaya Crystalline, Lesser Himalaya Crystalline and Lesser Himalaya Sequence, respectively. WGC: Wangtu Gneissic Complex. Geological setting is based on Sharma (1977); Vannay et al., (2001); Kumar et al., (2019b). The red dashed circle in the inset represents the region within 100 km radius from the Satluj River (marked as blue line) that was used to determine the earthquake distribution in the area. KCF in inset refers to Kaurik-Chango Fault. The numbers 1-44 refer to serial number of landslides.



**Fig. 2** Field photographs of some of the landslides (a) Khokpa landslide (S.N.1); (b) Akpa\_III landslide (S.N. 5); (c) Rarang landslide (S.N. 6); (d) Pawari landslide (S.N.14); (e) Urni landslide (S.N.19); (f) Barauni Gad\_I\_S landslide(S.N. 38).Black circle in the pictures that encircles the vehicle is intended to represent the relative scale.

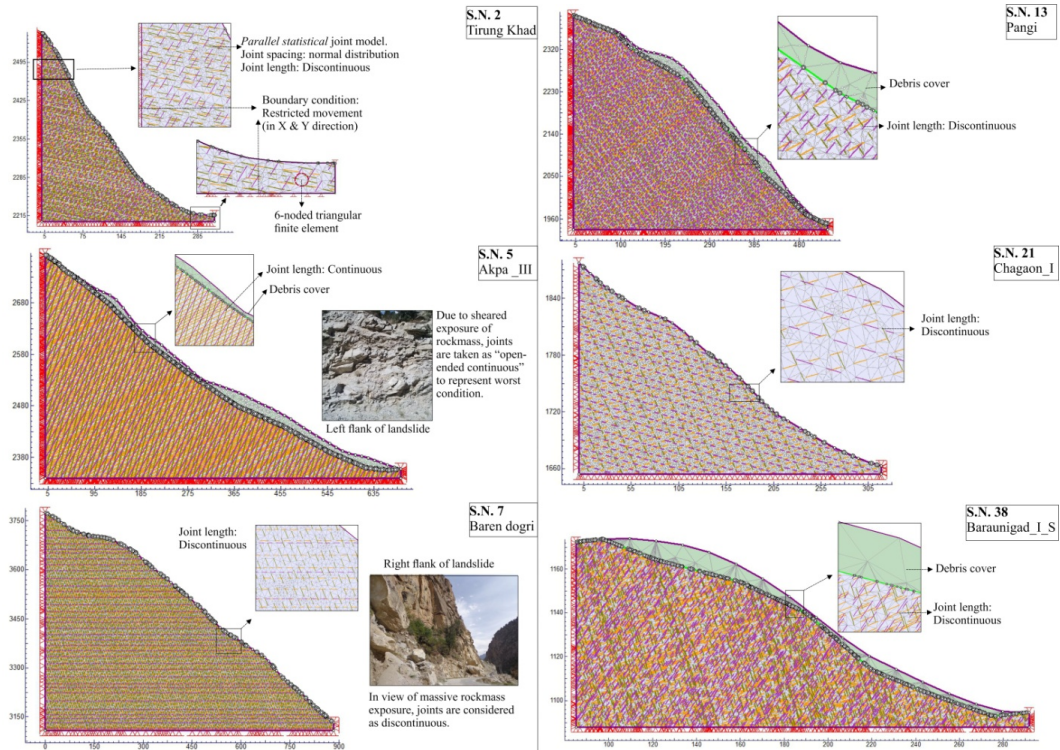


**Fig. 3** The FEM configuration of some of the slope models. S.N. refers to serial no. of landslides in Table 1. The joint distribution model in all the slopes was parallel statistical with normal distribution of joint spacing.

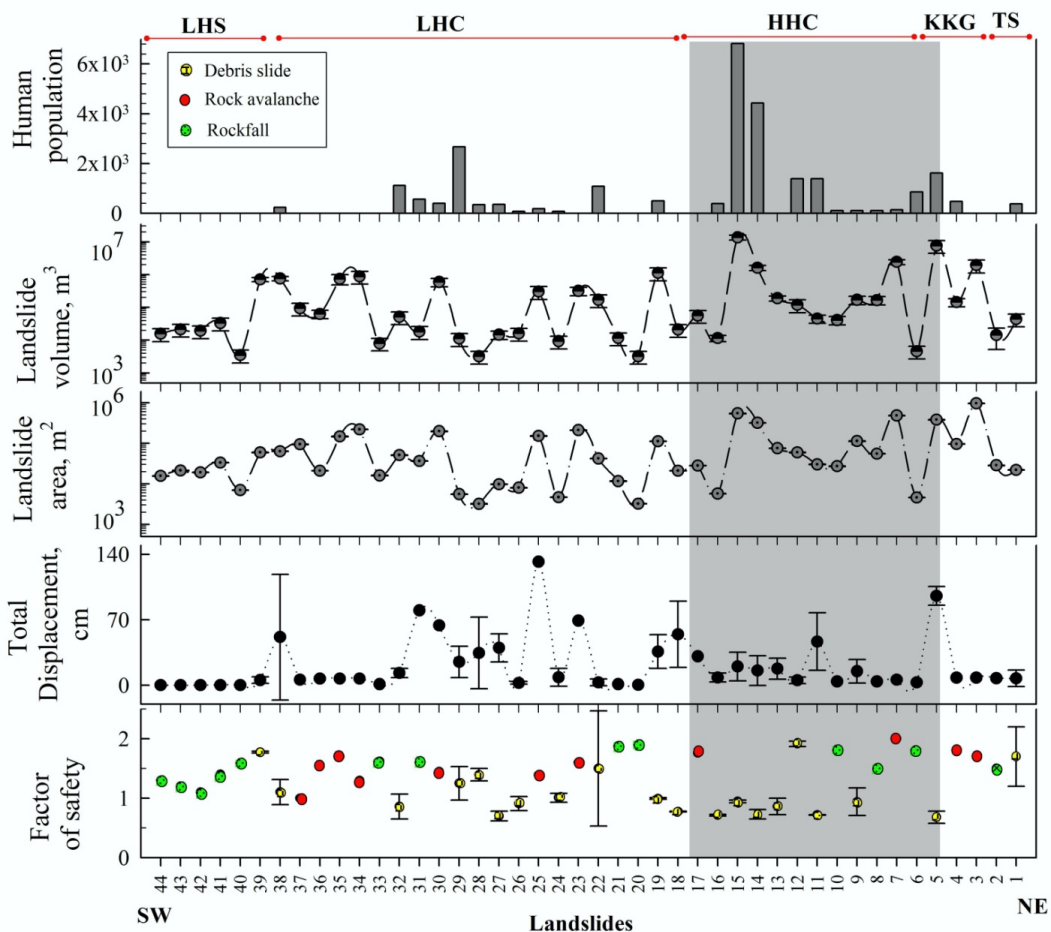


**Fig. 4** The FEM analysis of all forty-four landslides. Grey bar in the background highlights the Higher Himalaya Crystalline (HHC) region that comprises relatively more unstable landslides, relatively more landslide volume and human population. Source of human population: Census 2011 (Govt. of India, New Delhi). TS, KKG, HHC, LHC and LHS are Tethyan Sequence, Kinnaur Kailash Granite, Higher Himalaya Crystalline, Lesser Himalaya Crystalline and Lesser Himalaya Sequence, respectively

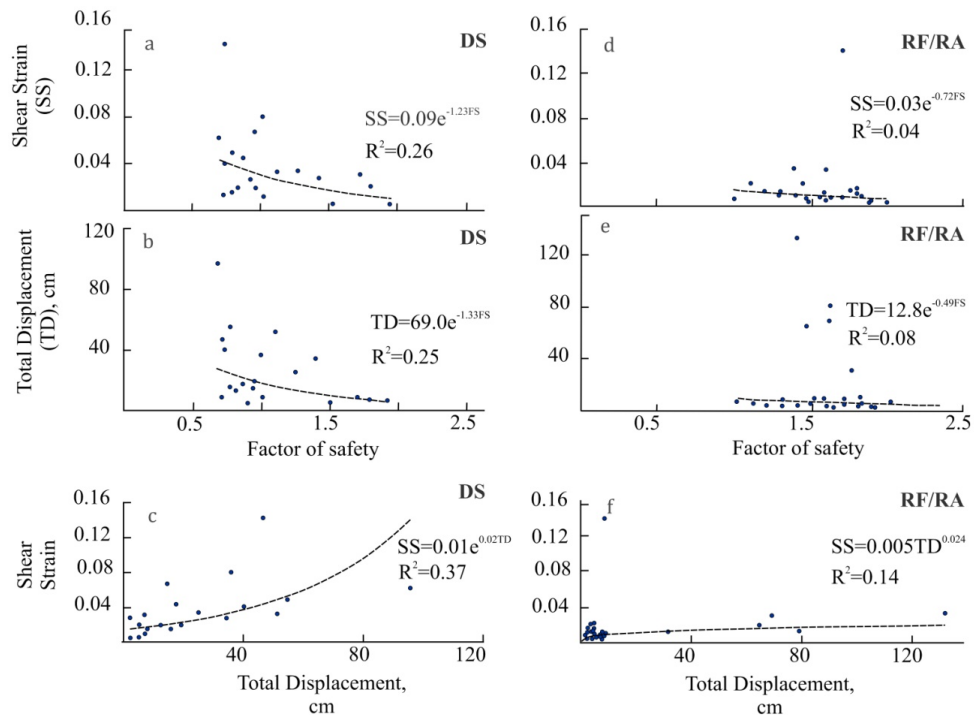


**Fig. 5** Relationship of Factor of Safety (FS), Total Displacement (TD) and Shear Strain (SS). DS, RF, and RA refer to Debris slide, rock fall and rock avalanche, respectively.

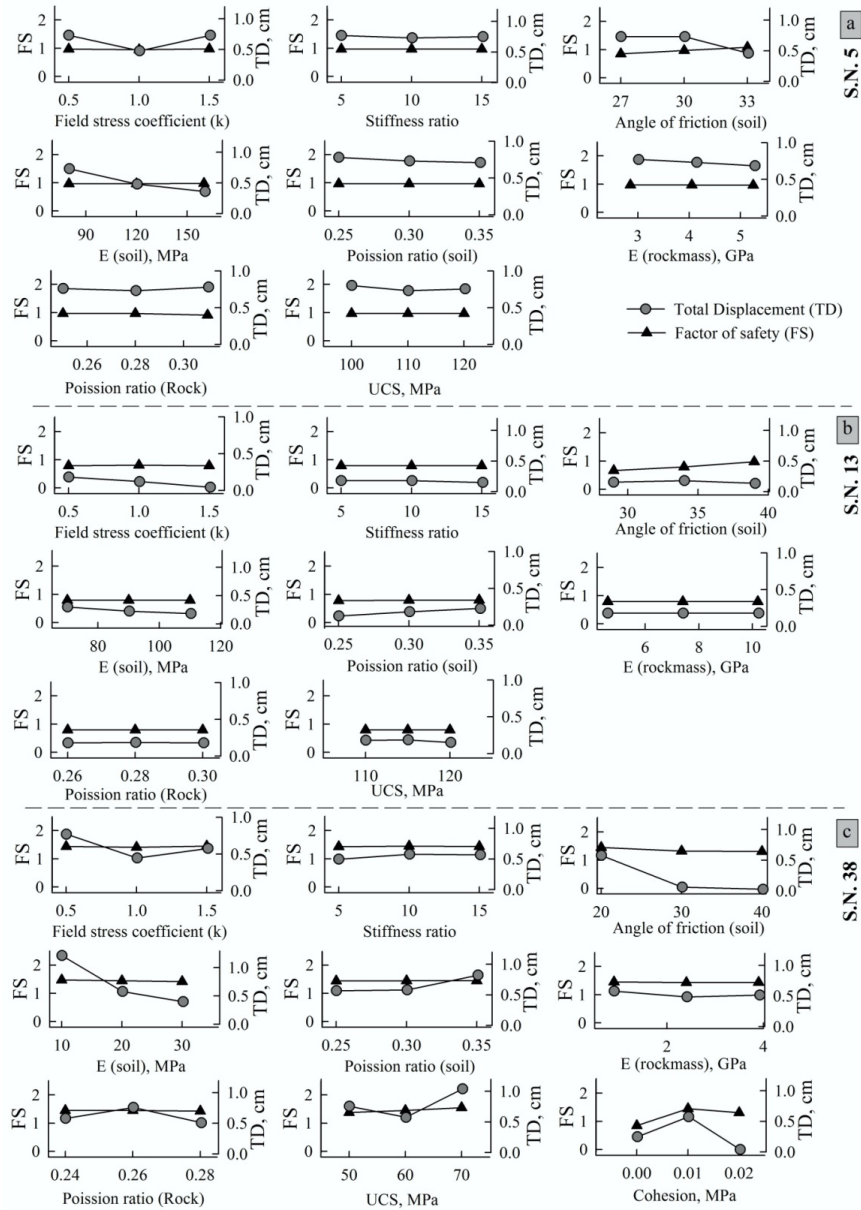


**Fig. 6** Parametric analysis of debris slides. (a) Akpa\_III (S.N. 5): (b) Pangl\_III (S.N. 13): (c) Barauni Gad\_I\_S (S.N. 38). S. N. refers to serial no. of landslides in Table 1.

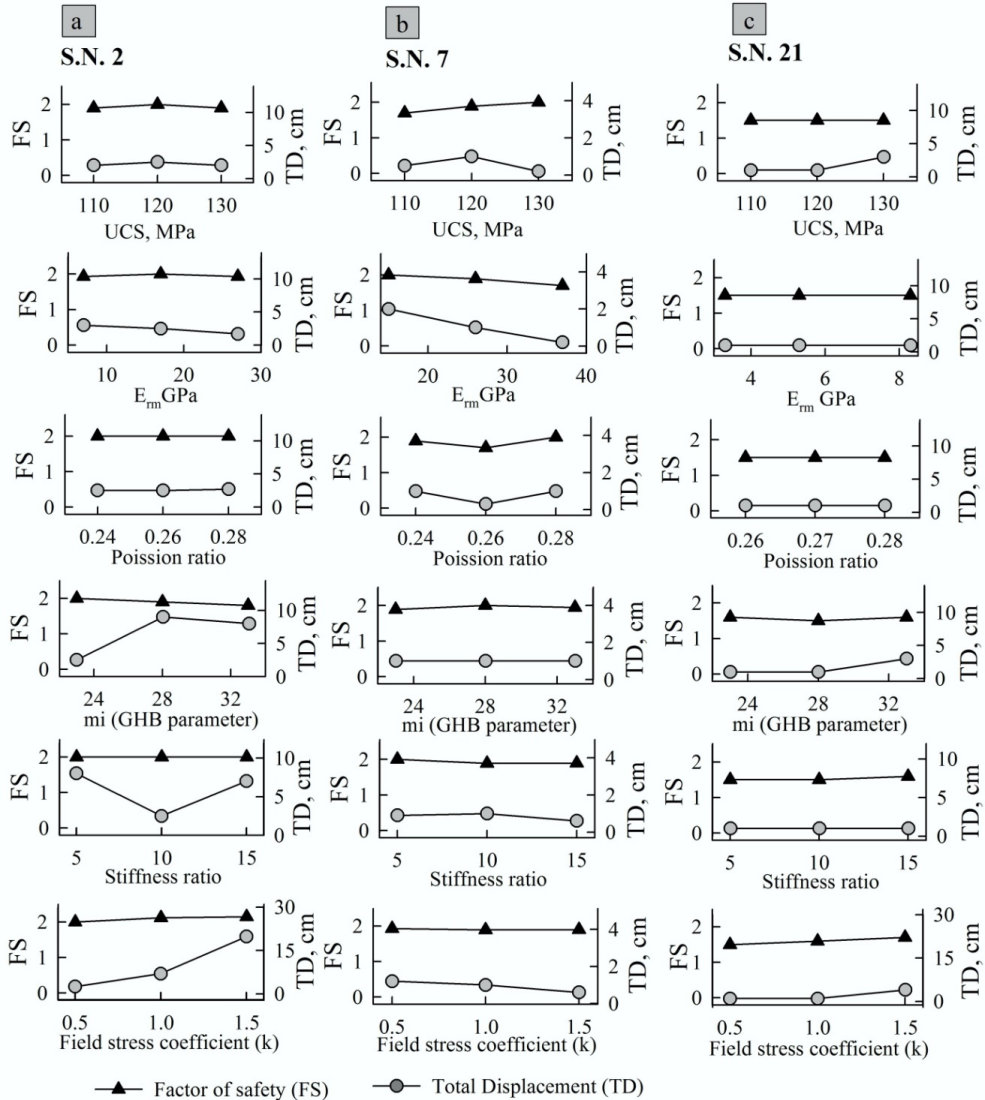


**Fig. 7** Parametric analysis of rockfall/rock avalanche. (a) Tirung khad (S.N. 2); (b) Baren Dogri (S.No. 7); (c) Chagaon\_II (S.N. 21).

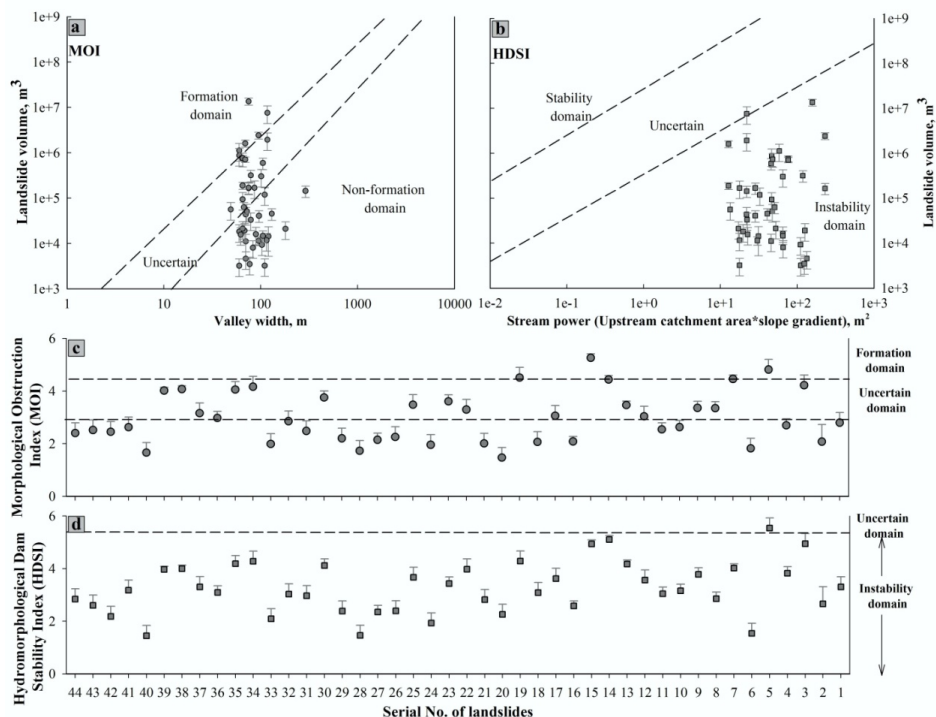


**Fig. 8** Landslide damming indices (a) Morphological Obstruction Index (MOI); (b) Hydromorphological dam stability index (HDSI); (c) Landslides vs. MOI; (d) Landslides vs. HDSI.

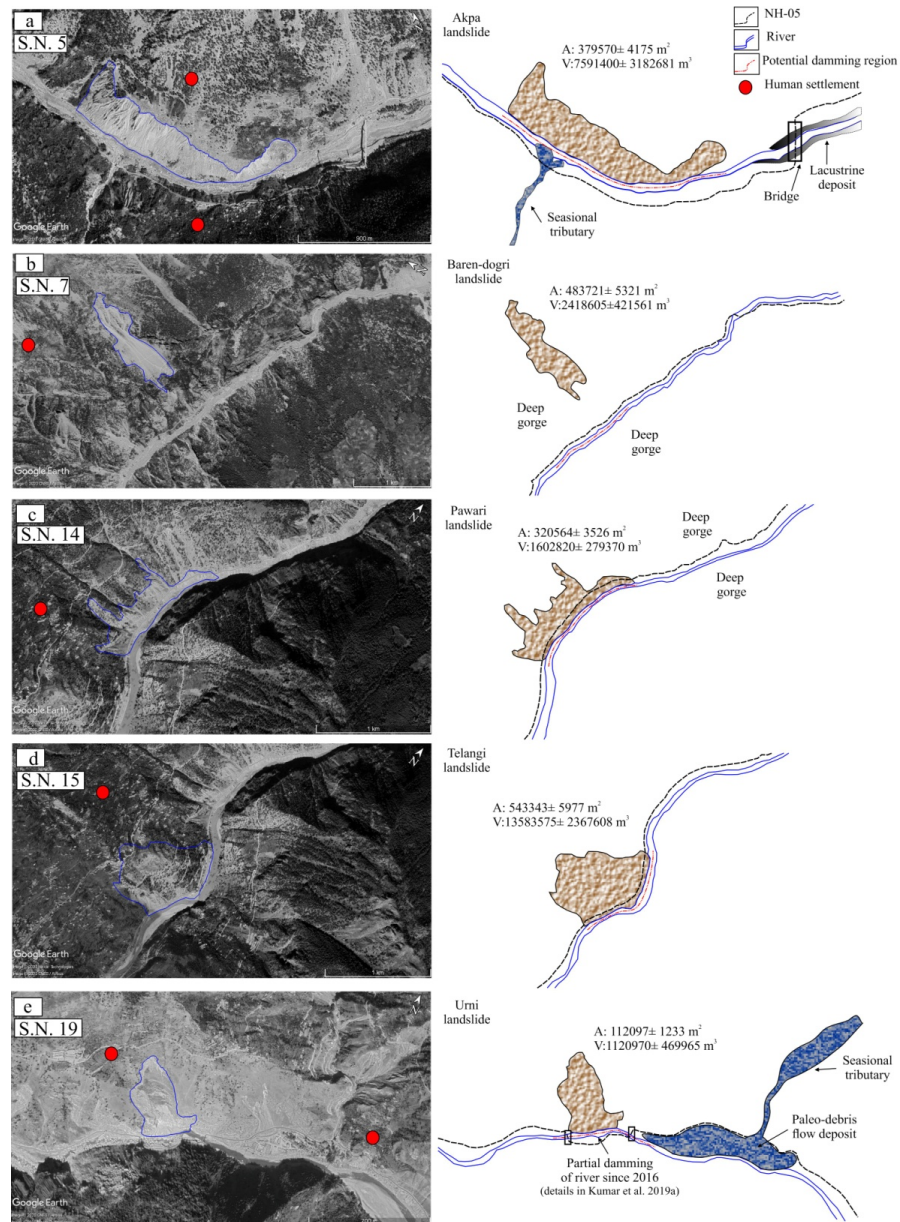


**Fig. 9** Potential landslide damming locations. (a) Akpa\_III landslide; (b) Baren dogri landslide; (c) Pawari landslide; (d) Telangi landslide; (e) Urni landslide. S. N. refers to serial no. of landslides in Table 1.

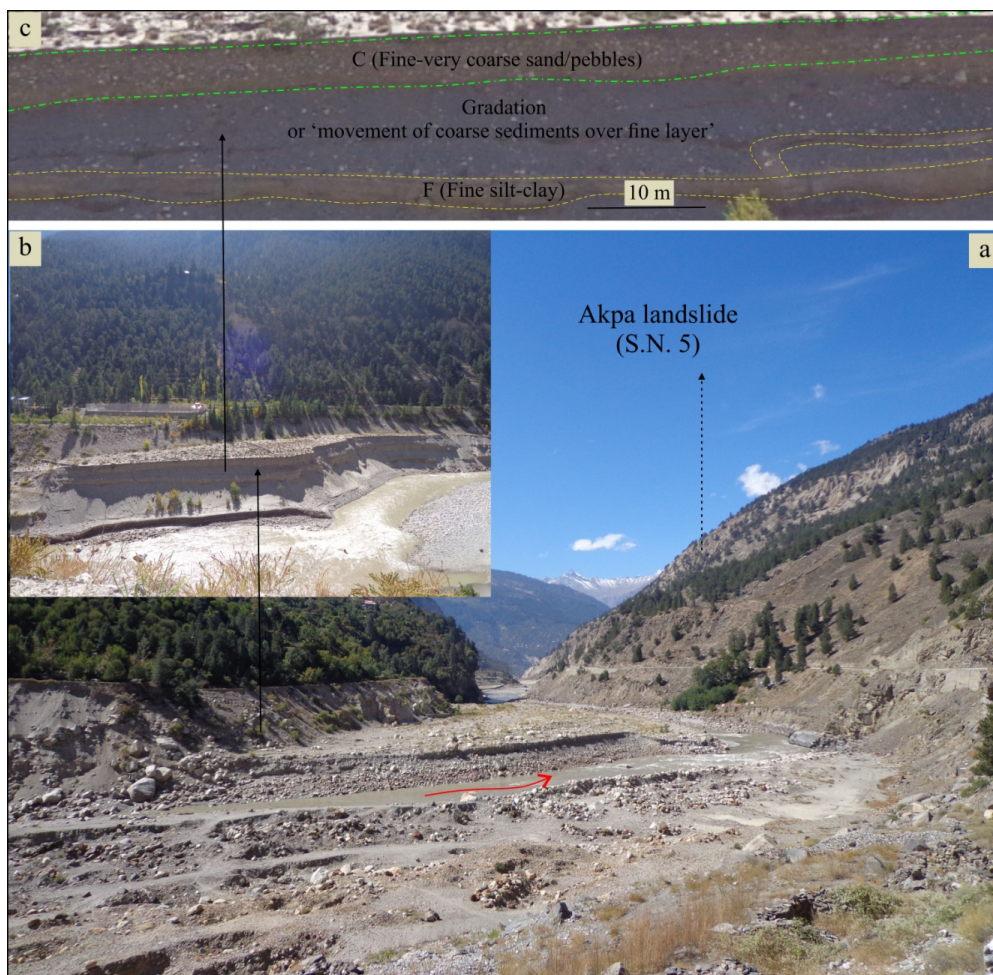


**Fig. 10** Field signatures of the landslide damming near Akpa\_III landslide. (a) Upstream view of Akpa landslide with lacustrine deposit at the left bank; (b) enlarged view of lacustrine deposit with arrow indicating lacustrine sequence; (c) alternating fine-coarse sediments. F and C refer to fine (covered by yellow dashed lines) and coarse (covered by green dashed lines) sediments, respectively.

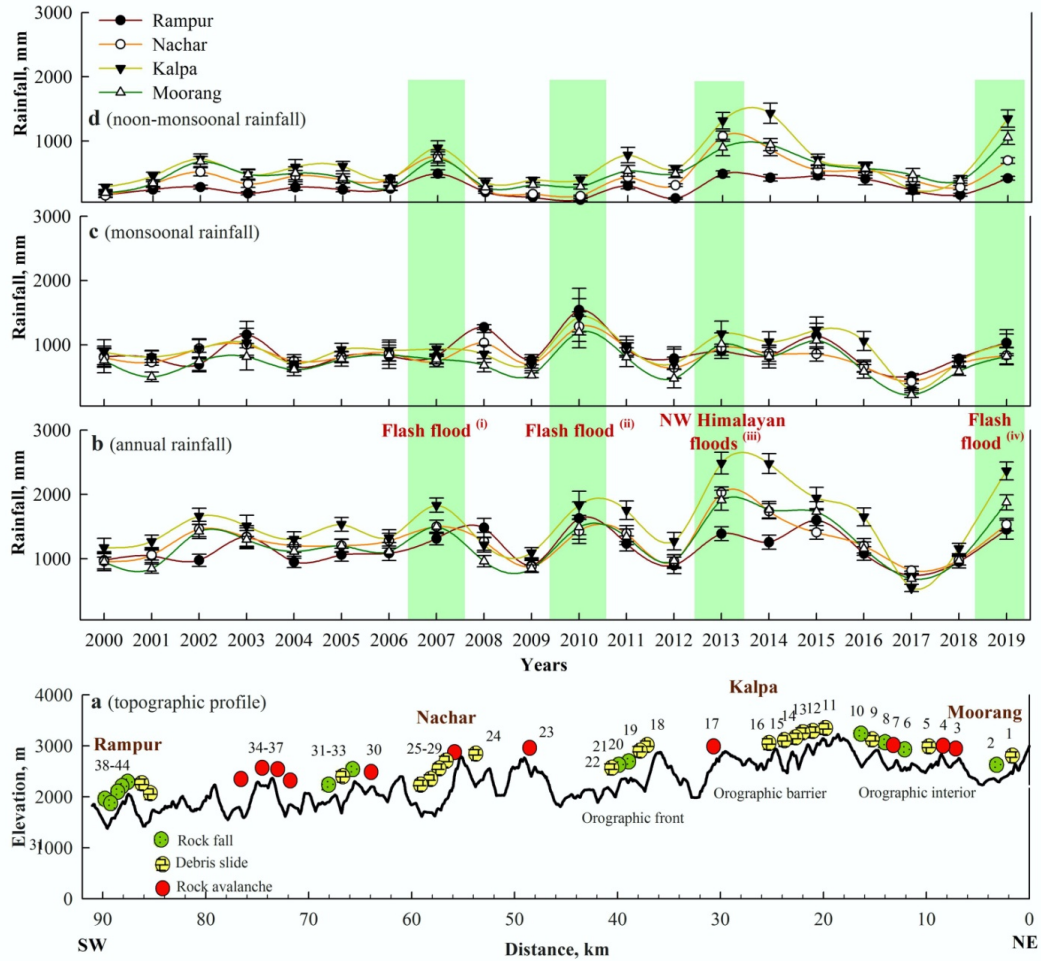


**Fig. 11** Rainfall distribution. (a) Topographic profile; (b) annual rainfall; (c) monsoonal (June-Sep.) rainfall; (d) non-monsoonal (Oct.-May) rainfall. Green bars represent years of relatively more rainfall resulting into flash floods, landslides and socio-economic loss in the region. (i):hpervis.nic.in, retrieved on March 1, 2020; Department of Revenue, Govt. of H.P. (ii): hpervis.nic.in, retrieved on March 1, 2020.(iii): Kumar et al., 2019a;ndma.gov.in, retrieved on march 1, 2020 (iv):sandrp.in, retrieved on march 1, 2020.The numbers 1-44 refer to serial number of landslides.

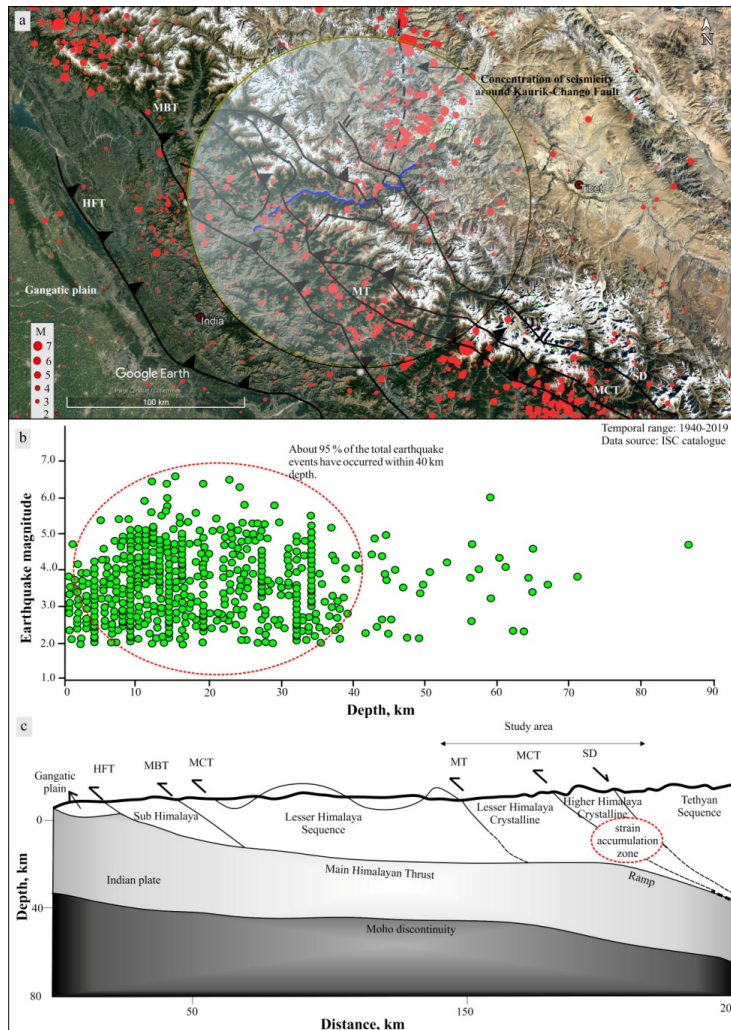


**Fig. 12** Earthquake distribution. (a) Spatial variation of earthquakes. The transparent circle represents the region within 100 km radius from the Satluj River (blue line). The black dashed line represents the seismic dominance around Kaurik-Chango fault; (b) earthquake magnitude vs. focal depth. The red dashed region highlights the concentration of earthquakes within 40 km depth. ISC: International Seismological Centre; (c) Cross section view (Based on Hazarika et al. 2017; Bilham, 2019). Red dashed circle represents the zone of strain accumulation caused by the Indian and Eurasian plate collision. SD, MCT, MT, MBT and HFT are Sangla Detachment, Main Central Thrust, Munsiari Thrust, Main Boundary Thrust and Himalayan Frontal Thrust, respectively.

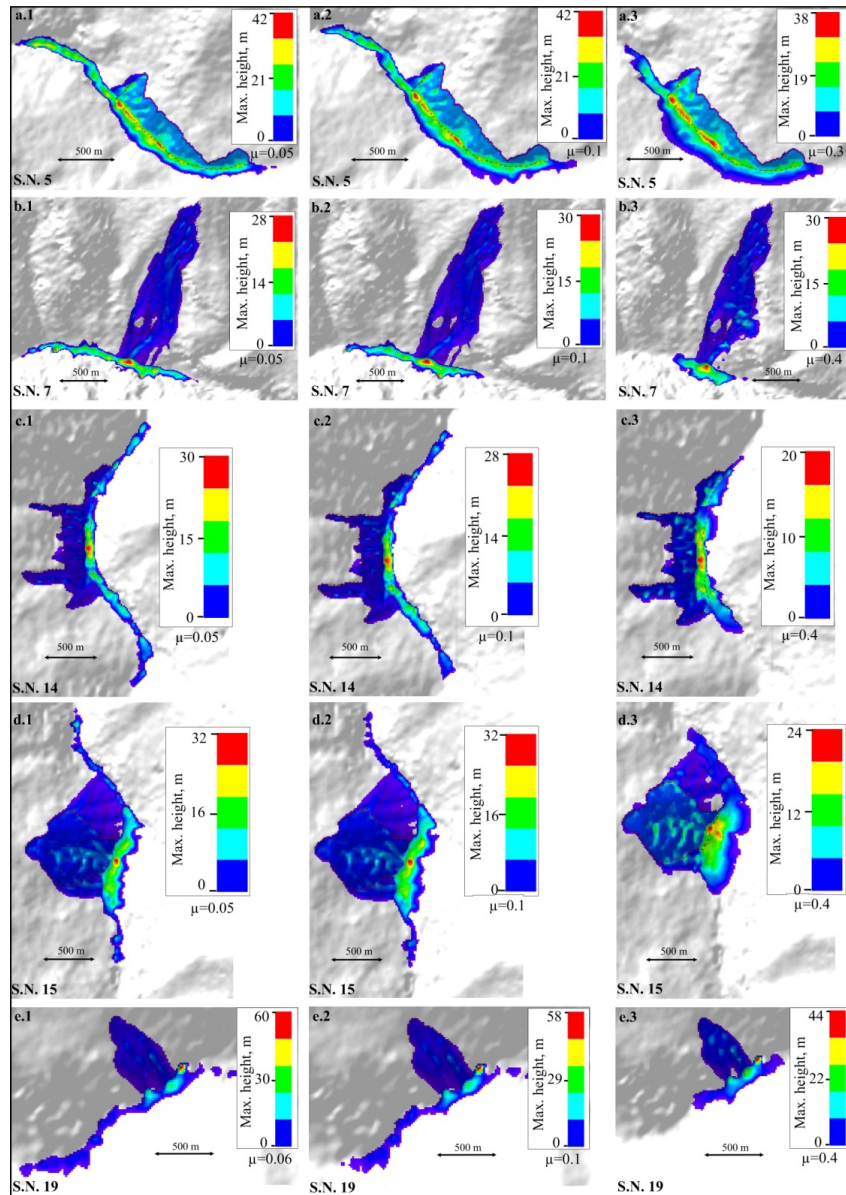


**Fig. 13** Results of run-out analysis.  $\mu$  refers to coefficient of friction. S. N. refers to serial no. of landslides in Table 1

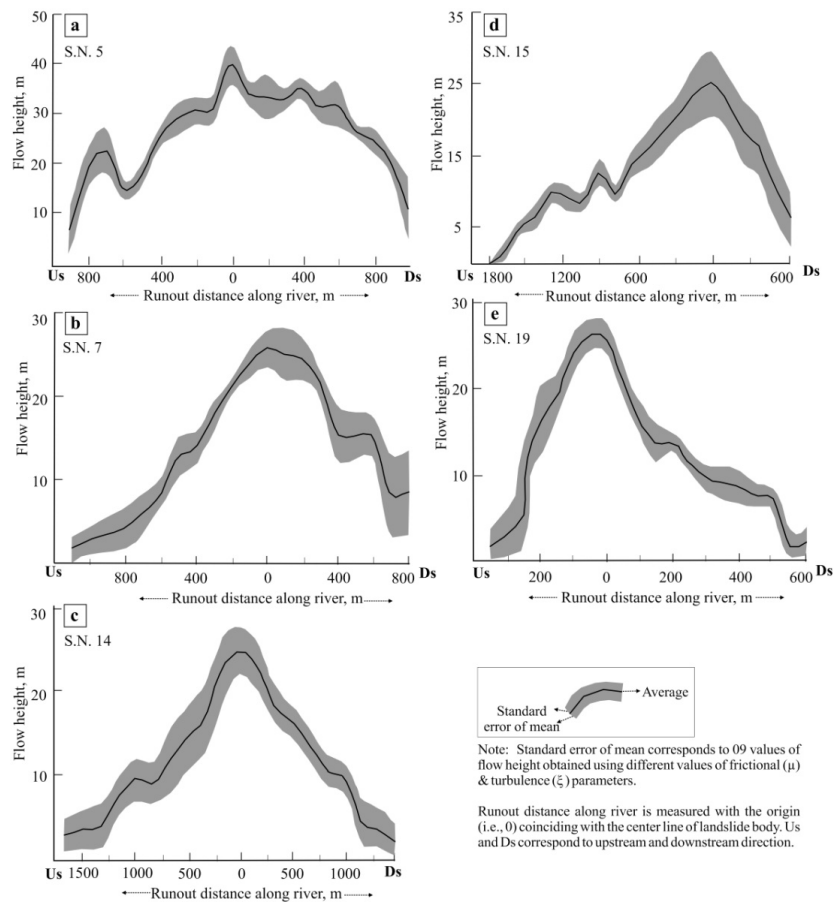


**Fig. 14** Results of run-out analysis at different values of  $\mu$  and  $\xi$ .  $\mu$  and  $\xi$  refer to coefficient of friction and turbulence, respectively.